4.1.1.4 Solar photosphere and chromosphere

Matthias Steffen

Traditionally, the atmosphere of the Sun has been divided into four layers, starting with the *photosphere* at the bottom, followed by the *chromosphere*, the *transition region*, and the *corona* as the outermost region.

The *photosphere* is a layer of only a few hundred kilometers thickness in which the temperature drops outwards from around 6000 K at the solar "surface" to around 4000 K at the "temperature minimum". The photospheric gas changes from almost completely opaque at the bottom to almost completely transparent just a little more than one hundred kilometers higher up. Virtually all light which we receive from the Sun originates in the photosphere. Hence, most of the information we have about the Sun is derived from observations of this thin layer.

Above the "temperature minimum", the temperature appears to rise again, first gently – forming the chromospheric plateau – and then very steeply in the transition region at a height of about 2000 km above the solar "surface". The *chromosphere* is thus defined as the zone between the "temperature minimum" and the transition region. It has obtained its name from the colorful appearance it exhibits during a total solar eclipse. Hydrogen is partially ionized throughout the chromosphere, which is neither in radiative equilibrium (RE) nor in local thermodynamic equilibrium (LTE).

Increasingly detailed observations have revealed that the simple plane-parallel representation of the solar atmosphere outlined above is not tenable in any of its layers. In addition to being *spatially inhomogeneous* at almost all spatial scales, the solar atmosphere is also *highly dynamic* at almost all timescales.

For recent reviews on the solar atmosphere see [i, 0, 3, 4]. Particularly useful textbooks on this subject are [h, k].

4.1.1.4.1 Mean vertical temperature structure

This Section is dedicated to 1-dimensional models of the solar photosphere and chromosphere, covering both semi-empirical and theoretical models. While the temperature stratification of semi-empirical models is found by trial and error, the temperature structure of theoretical models is obtained by solving an *energy equation*. In the solar atmosphere, energy is not only transported by *radiation*, but also by *convection* (and convective "overshoot") in the photosphere, by *waves* in the chromosphere, and by *thermal conduction* and *ambipolar diffusion* in the transition region. Besides the "classical" static equilibrium models, time-dependent 1-dimensional hydrodynamical simulations have been employed to study the effect of acoustic waves on the structure, dynamics and energetics of the solar chromosphere.

4.1.1.4.1.1 Thermal structure of the lower photosphere from CLV

The fact that the transition from optically thin to optically thick conditions depends on the observed position on the solar disk and on wavelength – in a most pronounced way in a strong spectral line – allows us to derive empirical information about the thermodynamic structure of the low solar atmosphere. The observed center-to-limb variation (CLV) of the solar continuum intensity is a fundamental constraint for both semi-empirical and theoretical models of the solar photosphere. An overview of the measured CLV is presented graphically in Fig. 1. For 30 wavelengths between $\lambda\,303.327$ and $\lambda\,1098.950$ nm, a polynomial approximation

$$I_\lambda(\mu)/I_\lambda(1) \approx P_5(\lambda,\mu) = \sum_{k=0}^{5} A_k(\lambda)\,\mu^k\,, \quad \sum_{k=0}^{5} A_k(\lambda) = 1\,, \tag{1}$$

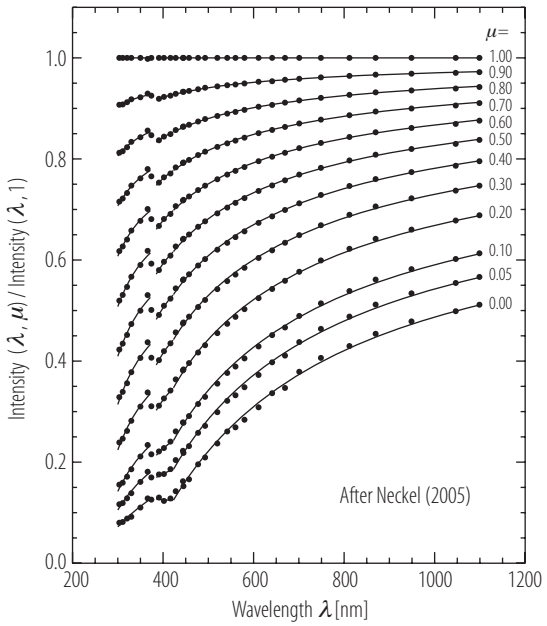

Fig. 1. Observed center-to-limb variation of the solar continuum intensity as a function of wavelength. Dots are computed from the 5th order polynomial approximation $P_5(\lambda, \mu)$ (Eq. 1) with coefficients listed in Table 1 according to [94Nec] for 30 wavelengths between λ 303.327 and λ 1098.950 nm. Continuous lines represent the analytical interpolation functions $p_5(\lambda, \mu)$ (Eq. 2) given by [05Nec] and listed in Table 2.

has been provided by [94Nec], where $\mu = \cos\theta$, θ being the angle between the normal to the solar surface and the line-of-sight ($\mu = 1$ at disk center, $\mu = 0$ at the limb). The coefficients $A_0 \ldots A_5$ given by [94Nec] are reproduced in Table 1. Except for a narrow region around the Balmer jump between 372.98 and 385 nm, the coefficients $A_0 \ldots A_5$ can be reasonably well approximated as a function of wavelength as

$$A_k(\lambda) \approx a_k(\lambda) = a_{k0} + \frac{a_{k1}}{\lambda} + \frac{a_{k5}}{\lambda^5}\,, \quad P_5(\lambda,\mu) \approx p_5(\lambda,\mu) = \sum_{k=0}^{5} a_k(\lambda)\,\mu^k\,. \tag{2}$$

The coefficients a_{k0}, a_{k1}, and a_{k5} are tabulated in Table 2.

For a plane-parallel (1-dimensional) atmosphere, the emergent intensity is given by

$$I_\lambda(\mu) = \int_0^\infty S_\lambda(\tau_\lambda)\exp\{-\tau_\lambda/\mu\}\,\mathrm{d}\tau_\lambda/\mu\,, \tag{3}$$

where $S_\lambda = \epsilon_\lambda/\kappa_\lambda$ is the (monochromatic) source function, i.e the ratio of total emissivity to total opacity, and τ_λ is the (monochromatic) optical depth defined as

$$\tau_\lambda(z) = \int_z^\infty \rho(z')\,\kappa_\lambda(z')\,\mathrm{d}z' \quad \rho: \text{mass density}, \quad z: \text{geometric height, increasing upward.} \tag{4}$$

Here ρ is the mass density, κ_λ is the opacity per unit mass, and z is the geometric height (increasing upward). For a given limb darkening law $I_\lambda(\mu)$, Eq. (3) constitutes an integral equation of the first kind for the unknown source function $S_\lambda(\tau_\lambda)$. In fact, defining $\xi = \ln\mu$ and $\eta = \ln\tau_\lambda$, the relation between $I_\lambda(\mu)$ and $S_\lambda(\tau_\lambda)$ can be written as a convolution [53Syk]:

$$I_\lambda(\xi) = \int_0^\infty S_\lambda(\eta)\,g(\xi-\eta)\,\mathrm{d}\eta\,, \quad \text{with} \quad g(x) = \exp\{-x-\exp(-x)\}\,, \tag{5}$$

Table 1. Coefficients of limb-darkening functions $P_5(\lambda, \mu)$ as defined in Eq. (1), reproduced from [94Nec].

λ [nm]	A_0	A_1	A_2	A_3	A_4	A_5
303.327	0.08011	0.70695	0.49910	−0.31080	−0.02177	0.04642
310.843	0.08160	0.71609	0.69685	−0.87703	0.47008	−0.08760
320.468	0.08833	0.77285	0.65382	−1.04647	0.72921	−0.19775
329.897	0.09188	0.92459	0.19604	−0.39546	0.23599	−0.05303
349.947	0.11012	1.02168	−0.10924	−0.00055	−0.08688	0.06487
365.875	0.12828	1.04969	0.17482	−1.13371	1.23882	−0.45990
374.086	0.12579	0.85402	0.54601	−1.15048	0.88928	−0.26462
390.915	0.12995	0.91836	−0.07566	0.19149	−0.28712	0.12298
401.970	0.12323	1.08648	−0.43974	0.45912	−0.32759	0.09850
416.319	0.12814	1.19947	−0.84407	1.07201	−0.79537	0.23982
427.930	0.14249	1.28796	−1.19564	1.68603	−1.36658	0.44572
443.885	0.16220	1.24893	−0.92165	0.89978	−0.50148	0.11220
445.125	0.15248	1.38517	−1.49615	1.99886	−1.48155	0.44119
457.345	0.16604	1.38544	−1.52275	2.00232	−1.45969	0.42864
477.427	0.19571	1.30551	−1.25845	1.50626	−1.05472	0.30570
492.905	0.20924	1.30798	−1.20411	1.21505	−0.67196	0.14381
519.930	0.23695	1.29927	−1.28034	1.37760	−0.85054	0.21706
541.760	0.26073	1.27428	−1.30352	1.47085	−0.96618	0.26384
559.950	0.26892	1.34319	−1.58427	1.91271	−1.31350	0.37295
579.880	0.28392	1.36896	−1.75998	2.22154	−1.56074	0.44630
610.975	0.30854	1.36620	−1.83572	2.33221	−1.63082	0.45959
640.970	0.33644	1.30590	−1.79238	2.45040	−1.89979	0.59943
669.400	0.34685	1.37539	−2.04425	2.70493	−1.94290	0.55999
700.875	0.37885	1.25553	−1.70908	2.19647	−1.59554	0.47378
748.710	0.40627	1.22842	−1.67877	2.05535	−1.39972	0.38845
811.760	0.42977	1.25182	−1.85164	2.31949	−1.59101	0.44155
869.600	0.45396	1.25101	−2.02958	2.75410	−2.02287	0.59338
948.850	0.47855	1.19813	−1.86296	2.36939	−1.64367	0.46056
1046.600	0.49870	1.21429	−2.06976	2.80703	−2.05247	0.60221
1098.950	0.51149	1.19354	−2.00174	2.66936	−1.94981	0.57715

Table 2. Coefficients of the approximate limb-darkening functions $p_5(\lambda, \mu)$ as defined in Eq. (2), reproduced from [05Nec].

λ [nm]	a_{00}	a_{10}	a_{20}	a_{30}	a_{40}	a_{50}
–	a_{01}	a_{11}	a_{21}	a_{31}	a_{41}	a_{51}
range	a_{05}	a_{15}	a_{25}	a_{35}	a_{45}	a_{55}
300.00	0.356010	1.115290	−0.672370	0.186960	0.000380	0.013730
to	−0.085217	0.085217	–	–	–	–
372.98	–	−0.001871	0.003589	−0.002415	0.000897	−0.000200
385.00	0.099000	1.968840	−2.805110	3.327800	−2.178780	0.588250
to	0.010643	−0.010643	–	–	–	–
422.57	–	−0.009166	0.024873	−0.029317	0.018273	−0.004663
422.57	0.752670	0.938740	−1.892870	2.422340	−1.711500	0.490620
to	−0.265577	0.265577	–	–	–	–
1100.00	–	−0.004095	0.012582	−0.017117	0.011977	−0.003347

showing that the solution of Eq. (3) essentially poses the same challenges as the well known "deconvolution problems".

If the source function is written as a polynomial in τ_λ,

$$S_\lambda(\tau_\lambda) = I_\lambda(1) \sum_{k=0}^{5} A_k(\lambda)\, \tau_\lambda^k/(k!)\,, \tag{6}$$

the straightforward integration of Eq. (3) results in just the same polynomial representation of $I_\lambda(\mu)$ as given by Eq. (1): Measurement of the limb-darkening coefficients $A_k(\lambda)$ immediately yields the depth dependence of the source function. For a linear source function, we recover the Eddington-Barbier relation, $I_\lambda(\mu) = S_\lambda(\tau_\lambda{=}\mu)$, but higher-order terms destroy the simple one-to-one relation between I_λ and S_λ. Moreover, even slight errors in the higher-order limb-darkening coefficients may cause large, spurious fluctuations in the corresponding τ-dependence of the source function. Since reliable limb-darkening curves are restricted to the range $0.1 < \mu < 1$, it is clear that such measurements can only probe the rather limited optical depth range $0.1 < \tau_\lambda < 1$.

In the continuum forming layers, local thermodynamic equilibrium (LTE) is a valid approximation, so the source function equals the Planck Function,

$$S_\lambda = B_\lambda = \frac{2\,h\,c^2}{\lambda^5}\,\frac{1}{\exp\{(h\,c)/(\lambda\,k\,T)\} - 1} \tag{7}$$

(h: Planck constant, c: speed of light, k: Boltzmann constant, T: temperature). All intensities can be converted to an absolute scale by noting that the 'limb temperature', T_0, is identical for all wavelengths. According to [05Nec], $T_0 = 4746$ K, which implies

$$I_\lambda(\mu \to 0) = B_\lambda(T_0)\,, \quad \text{hence} \quad I_\lambda(1) = B_\lambda(T_0)/A_0(\lambda) \quad \text{for all } \lambda\,. \tag{8}$$

For each wavelength, the empirical temperature stratification is then given by

$$T(\tau_\lambda) = q_\lambda \left\{ \ln\left(1 + \frac{\exp(q_\lambda/T_0) - 1}{u_\lambda(\tau_\lambda)}\right)\right\}^{-1} \tag{9}$$

where $q_\lambda = 1.43873 \times 10^7/\lambda$ (with wavelength λ in [nm]), and

$$u_\lambda(\tau_\lambda) \equiv \frac{S_\lambda(\tau_\lambda)}{B_\lambda(T_0)} = \frac{1}{A_0(\lambda)} \sum_{k=0}^{5} A_k(\lambda)\, \tau_\lambda^k/(k!)\,. \tag{10}$$

Alternative analytical representations of the measured limb-darkening curves using physically more 'reasonable' functions have been investigated by [96Nec] and [98Hes]. However, in a later publication [03Nec] found the 'physically more realistic' limb darkening functions to be not necessarily superior to the traditional polynomial representation, at least for extrapolation towards the very limb. The role of instrumental stray light in the context of high-precision limb darkening measurements aiming at the detection of long-term time variability of the photospheric temperature structure has recently been discussed by [07Els]. No such variability of the quiet solar photosphere with the activity cycle has yet been identified [03Liv]. Also, within the experimental uncertainties, no north-south asymmetry of the solar brightness distribution has been found [08Liv].

Precise measurements of the continuum brightness distribution across the solar disk over a wide range of wavelengths also allow the empirical determination of the (relative) wavelength dependence of the continuous opacity κ_λ at different heights (temperature) in the solar atmosphere. For this purpose, the quantity

$$\frac{\partial \tau_\lambda}{\partial T} = \kappa_\lambda\,\rho \left(\frac{\partial T}{\partial z}\right)^{-1} = \frac{q_\lambda}{T^2}\,\frac{u_\lambda(\tau_\lambda)}{v_\lambda(\tau_\lambda)}\,\frac{u_\lambda(\tau_\lambda) + x_\lambda}{x_\lambda}\,, \quad x_\lambda \equiv \exp(q_\lambda/T_0) - 1\,, \quad v_\lambda \equiv \frac{\partial u_\lambda}{\partial \tau_\lambda} \tag{11}$$

must be evaluated at constant T (for details see e.g. [59Gol]). Such investigations have shown that the continuous opacity in the solar atmosphere is mainly due to H^- and H, at least in the range 360 nm $< \lambda <$ 2500 nm [a].

4.1.1.4.1.2 1D LTE semi-empirical models of the solar photosphere

In order to derive a complete semi-empirical model atmosphere, the $T(\tau)$-relation is augmented with the theoretical requirement of hydrostatic equilibrium, sometimes including turbulent pressure:

$$\frac{\partial}{\partial \tau_\lambda}\left(P_\mathrm{g} + P_\mathrm{tur} + P_\mathrm{rad}\right) = \frac{\partial P_\mathrm{tot}}{\partial \tau_\lambda} = \frac{g}{\kappa_\lambda}\,, \tag{12}$$

where g is the solar surface gravity, κ_λ is the opacity per unit mass, P_g is the gas pressure,

$$P_\mathrm{g} = (n_e + \sum_i n_i)\,k\,T\,, \quad n_e : \text{electron density} \quad n_i : \text{density of atom or ion}\,, \tag{13}$$

P_tur is the turbulent pressure,

$$P_\mathrm{tur} = \frac{\rho}{2}\xi_\mathrm{tur}^2\,, \quad \rho : \sum_i (n_i\,m_i)\,, \quad m_i : \text{particle mass}\,, \quad \xi_\mathrm{tur} : \text{turbulent velocity}\,, \tag{14}$$

and P_rad is the radiation pressure,

$$\frac{\partial P_\mathrm{rad}}{\partial \tau_\lambda} \approx \frac{\sigma}{c}\,T_\mathrm{eff}^4\,, \quad \sigma : \text{Stefan-Boltzmann constant}\,, \quad T_\mathrm{eff} : \text{effective temperature}\,. \tag{15}$$

Given $T(\tau_\lambda)$, $\xi_\mathrm{tur}(\tau_\lambda)$, and adopting an equation of state, $\rho(P_\mathrm{g}, T)$ as well as an opacity law, $\kappa_\lambda(P_\mathrm{g}, T)$, Eq. (12) can be integrated inwards to obtain a complete model. This model is then used for the computation of synthetic spectra for comparison with observations. The $T(\tau)$-relation is adjusted until a chosen set of observed properties is reproduced. Apart from the continuum intensities (Sect. 4.1.1.4.1.1), the information contained in the spectral lines of various strength must be exploited to extend the height range covered by the semi-empirical approach.

One of the most successful semi-empirical models of the solar photosphere was derived by [67Hol], based on measurements of the continuum intensity between λ 0.09 to 100 μm, and on the investigation of about 900 carefully selected absorption lines in the visible solar spectrum under the assumption of strict LTE (source function = Planck function, ionization/excitation balance given by the Saha-Boltzmann equation). In its updated version [74Hol], the Holweger-Müller (HM) atmosphere is still heavily used today, mainly as a reference for chemical abundance determinations. A modern adaption of the HM model, published in [02Cow], is reproduced in Table 3. Note that the column mass density m is computed as

$$m = P_\mathrm{tot}/g\,, \tag{16}$$

with a depth-independent turbulence velocity of $\xi_\mathrm{tur} = 1.0$ km/s for the calculation of the turbulent pressure P_tur. The (meteoritic) solar abundances from [98Gre] were adopted for the model's chemical composition.

The HM model has recently been modified by [99Gre] to achieve a consistent excitation- and ionization equilibrium of iron. The resulting iron abundance agrees with the meteoritic value.

4.1.1.4.1.3 1D non-LTE semi-empirical models of the solar chromosphere

The construction of a semi-empirical model of the higher atmospheric layers is increasingly more difficult because (i) it requires observational data beyond the visible spectral range (EUV, far IR), and (ii) the approximation of LTE breaks down and must be replaced by a full treatment of the statistical equilibrium problem (non-LTE approach) to derive the level populations of all ions, and in turn the opacities and the source function.

Based on these principles, a variety of semi-empirical models has been constructed over the last decades, covering the photosphere, chromosphere, transition region and base of the corona

Table 3. Holweger-Müller semi-empirical solar atmosphere, adapted from [02Cow].

$\log \tau_{500}$	$\log \kappa_{500}$ [cm^2 g^{-1}]	$\log \rho$ [g cm^{-3}]	$\log m$ [g cm^{-2}]	T [K]	$\log P_{\rm gas}$ [dyn cm^{-2}]	$\log N_e$ [cm^{-3}]
−6.54	−3.21233	−10.30487	−3.32664	3900	1.10517	9.38881
−6.39	−3.18006	−10.15745	−3.17822	3910	1.25310	9.53071
−6.23	−3.14267	−10.01913	−3.03809	3924	1.39305	9.66323
−6.08	−3.10089	−9.88807	−2.90514	3939	1.52595	9.78859
−5.93	−3.05389	−9.76371	−2.77877	3960	1.65196	9.90827
−5.77	−3.00441	−9.64551	−2.65777	3988	1.77401	10.02325
−5.62	−2.95117	−9.53269	−2.54123	4022	1.88997	10.13545
−5.47	−2.89347	−9.42343	−2.42906	4052	2.00303	10.24229
−5.31	−2.83654	−9.31114	−2.32043	4084	2.11093	10.34596
−5.16	−2.77650	−9.21667	−2.21513	4120	2.21696	10.44607
−5.01	−2.71422	−9.11822	−2.11259	4159	2.31890	10.54494
−4.85	−2.64995	−9.02123	−2.01265	4188	2.41896	10.63998
−4.70	−2.58519	−8.92702	−1.91507	4220	2.51706	10.73360
−4.55	−2.51971	−8.83476	−1.81942	4255	2.61300	10.82504
−4.39	−2.45247	−8.74400	−1.72543	4286	2.70697	10.91492
−4.24	−2.38531	−8.65482	−1.63305	4317	2.79900	11.00260
−4.09	−2.31749	−8.56655	−1.54192	4349	2.88997	11.08955
−3.93	−2.24949	−8.47978	−1.45186	4382	2.98100	11.17522
−3.78	−2.18230	−8.39383	−1.36272	4415	3.07004	11.26102
−3.63	−2.11334	−8.30857	−1.27429	4448	3.15806	11.34478
−3.47	−2.04460	−8.22366	−1.18659	4477	3.24601	11.42797
−3.32	−1.97510	−8.13930	−1.09953	4506	3.33304	11.51014
−3.17	−1.90623	−8.05567	−1.01306	4536	3.41996	11.59229
−3.02	−1.83773	−7.97265	−0.92691	4568	3.50596	11.67422
−2.86	−1.76802	−7.88941	−0.84122	4597	3.59095	11.75450
−2.71	−1.69897	−7.80660	−0.75572	4624	3.67697	11.83391
−2.56	−1.62949	−7.72400	−0.67068	4651	3.76200	11.91339
−2.40	−1.56083	−7.64187	−0.58573	4681	3.84702	11.99361
−2.25	−1.49201	−7.56019	−0.50086	4716	3.93202	12.07335
−2.10	−1.42297	−7.47873	−0.41609	4754	4.01703	12.15503
−1.94	−1.35477	−7.39816	−0.33137	4799	4.10106	12.23779
−1.79	−1.28643	−7.31749	−0.24657	4846	4.18611	12.32056
−1.64	−1.21803	−7.23792	−0.16185	4903	4.27091	12.40552
−1.48	−1.14856	−7.15852	−0.07720	4964	4.35603	12.49206
−1.33	−1.07998	−7.08035	0.00741	5040	4.43996	12.58252
−1.18	−1.00935	−7.00288	0.09184	5122	4.52504	12.67449
−1.02	−0.93667	−6.92665	0.17574	5217	4.60895	12.77151
−0.87	−0.86201	−6.85078	0.25888	5308	4.69197	12.86900
−0.72	−0.78225	−6.77754	0.34086	5416	4.77503	12.97428
−0.56	−0.68740	−6.70997	0.42030	5567	4.85400	13.10140
−0.41	−0.55972	−6.65267	0.49379	5781	4.92799	13.27300
−0.26	−0.39696	−6.60730	0.55772	6032	4.99198	13.48244
−0.10	−0.20908	−6.57398	0.61077	6315	5.04493	13.72057
0.05	−0.01122	−6.55098	0.65406	6617	5.08884	13.96727
0.20	0.16761	−6.53269	0.69044	6902	5.12516	14.18893
0.35	0.37876	−6.52462	0.72118	7266	5.15594	14.44871
0.51	0.59966	−6.52462	0.74604	7679	5.18099	14.71366
0.66	0.79064	−6.52593	0.76677	8059	5.20194	14.93666
0.81	0.92562	−6.52187	0.78606	8335	5.22089	15.08814
0.97	1.00775	−6.51089	0.80679	8500	5.24204	15.17955

Table 4. A selection of semi-empirical models of the average quiet solar atmosphere.

Authors	Scope	Observational basis	Ref.
		1D LTE models	
Holweger & Müller (1974)	photosphere	continua 0.09 ... 100 μm, $\approx$ 900 lines in visible spectrum	[74Hol]
Grevesse & Sauval (1999)	photosphere	65 Fe I lines in visible spectrum (modification of [74Hol] atmosphere)	[99Gre]
		1D non-LTE models	
Vernazza et al. (1981)	chromosphere	EUV continua 42 ... 132 nm (Skylab)	[81Ver]
Avrett (1985)	temperature - minimum	Ca H & K lines, UV & far IR continua	[85Avr]
Maltby et al. (1986)	photosphere - chromosphere	continua 0.3 ... 2.3 μm	[86Mal]
Fontenla et al. (1993)	transition - region	effect of ambipolar diffusion on H and He resonance lines	[90Fon, 91Fon] [93Fon]
Fontenla et al. (2006)	photosphere	continua 0.3 ... 10 μm	[99Fon, 06Fon]
Avrett & Loeser (2008)	chromosphere - transition region	EUV continua & lines (SUMER, HRTS spectra)	[08Avr]
		1D LTE multi-component models	
Ayres et al. (1986) 2-component model	photosphere - chromosphere	Ca H & K lines, IR CO bands λ 2.3 - 4.7 μm	[86Ayr]
Ayres et al. (2006) 6-component models	photosphere - chromosphere	visible / IR continuum intensities & CLV, IR CO bands λ 2.3 - 4.7 μm & CLV	[06Ayr]

(see Table 4 for an overview). One of the most prominent models of this kind is the VAL C model of Vernazza, Avrett & Loeser (1981) [81Ver]. It is based mainly on Skylab observations of the EUV continua (42 nm $< \lambda <$ 132 nm) and represents the average quiet Sun. Like all of its predecessors, it shows a temperature minimum near $\log \tau_{500} = -4$, and a chromospheric temperature rise (see Fig. 2). The models by Fontenla et al. [90Fon, 91Fon, 93Fon, 02Fon] eliminate the *ad hoc* temperature plateau in the upper chromosphere of the VAL models (outside the range of Fig. 2) by the more physical requirement of a balance between (i) downward energy transport from the corona by thermal conduction and ambipolar particle diffusion and (ii) the net radiative losses in these layers. The latest publication in this distinguished series of papers presents model VAL C7, which makes use of the SUMER atlas of the extreme ultraviolet spectrum of the Sun, and incorporates all previous improvements. It replaces the venerable VAL C model and is reproduced here in Table 5 (photosphere and lower chromosphere) and Table 6 (chromosphere and transition region) (see also Figs. 2 and 3). For completeness, the uppermost part of the VAL C7 model covering the transition region and lower corona is listed in Table 7.

These highly detailed models not only map out the physical structure of the mean solar atmosphere, but also provide information about the height of formation of the different continua (e.g. Fig. 3) and spectral lines (for details see [08Avr]). As illustrated in Fig. 4, the radiative energy losses of the chromospheric layers are dominated by a few strong emission lines of Ca II and Mg II, and by the continua of H I, H^-, and He I. In addition, millions of weak lines (line haze) make a considerable contribution. The radiative losses of the chromosphere must be compensated by some non-radiative heating mechanism to sustain the thermal structure of the semi-empirical models,

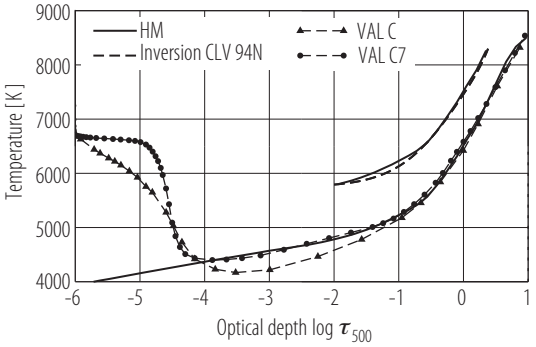

Fig. 2. Temperature structure on the optical depth scale τ_{500} of the Holweger-Müller (HM) semi-empirical model atmosphere as listed in Table 3 (solid), compared with the semi empirical models VAL C [81Ver] (filled triangles) and VAL C7 [08Avr] (filled circles) given in Table 5. The line segments shown in the range $-2 < \log \tau_{500} < 0.4$ are, respectively, the purely empirical temperature profile obtained from the inversion of the limb darkening measurements of [94Nec] according to Eqs. (9) and (10) (dashed), and the corresponding part of the HM temperature structure (solid), both shifted up by +1000 K for clarity.

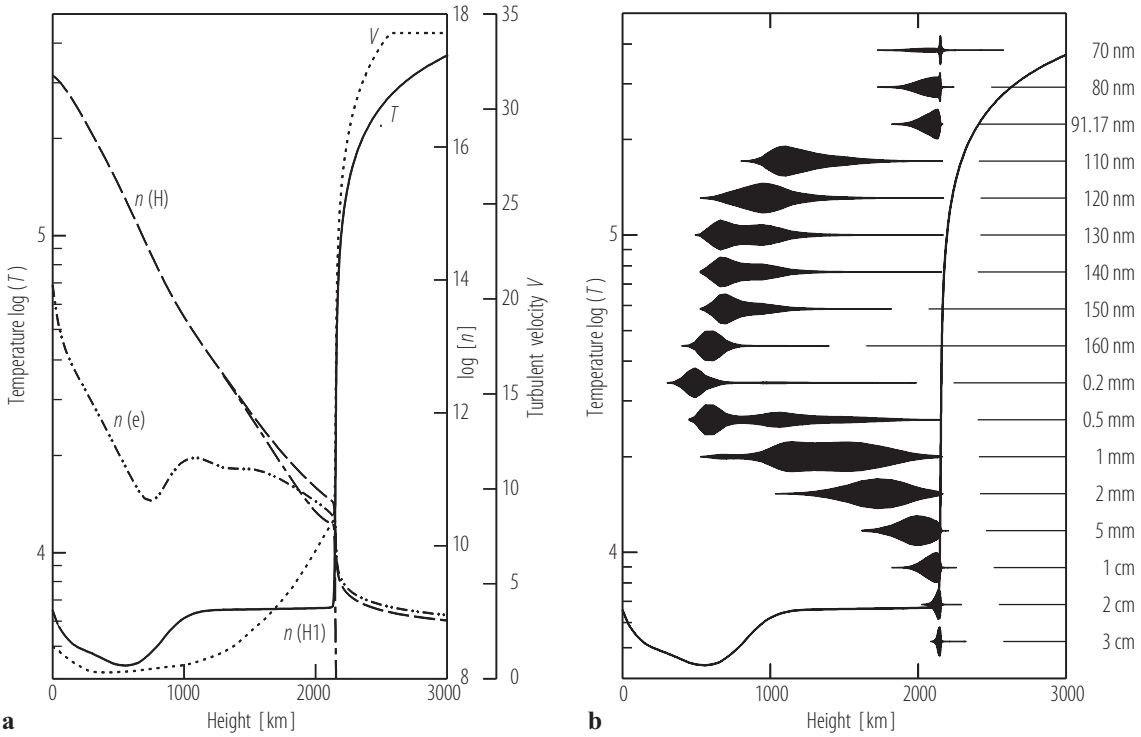

Fig. 3. Graphical representation of model VAL C7, reproduced from [08Avr]. **Left:** temperature T [K], turbulent velocity V [km/s], total hydrogen density n(H), neutral hydrogen density n(HI), and electron density n(e) [cm^{-3}] as a function of geometric height. **Right:** temperature distribution along with the contribution functions dI/dh of the continuum intensities at (from top to bottom) 70, 80, 91.17, 110, 120, 130, 140, 150, 160 nm in the extreme ultraviolet, and at radio wavelengths 0.2, 0.5, 1, 2, 5 mm, 1, 2, 3 cm.

Table 5. VAL C7 semi-empirical non-LTE model of the solar photosphere and lower chromosphere, adapted from [08Avr].

$\log \tau_{500}$	height [km]	$\log \rho$ [g cm^{-3}]	$\log m$ [g cm^{-2}]	T [K]	$\log P_{\rm gas}$ [dyn cm^{-2}]	$\log N_e$ [cm^{-3}]	$V_{\rm tur}$ [km s^{-1}]
−5.2990	1520.00	−11.66334	−4.38373	6623	0.02531	11.14799	2.575
−5.1701	1398.00	−11.32643	−4.08991	6610	0.33264	11.15473	1.803
−5.0764	1299.00	−11.05266	−3.83476	6598	0.59373	11.17231	1.390
−4.9914	1214.00	−10.81816	−3.60889	6576	0.82217	11.24551	1.159
−4.9073	1143.00	−10.61816	−3.41669	6531	1.01620	11.30103	0.990
−4.8523	1101.00	−10.49648	−3.30120	6474	1.13226	11.32469	0.896
−4.8038	1065.00	−10.38913	−3.20073	6400	1.23350	11.32222	0.823
−4.7590	1032.00	−10.28811	−3.10707	6315	1.32756	11.30750	0.765
−4.7203	1003.00	−10.19702	−3.02338	6225	1.41162	11.28149	0.719
−4.6788	971.00	−10.09307	−2.92922	6100	1.50596	11.23905	0.688
−4.6484	946.00	−10.00771	−2.85387	5969	1.58127	11.18127	0.672
−4.5971	900.00	−9.84497	−2.71063	5720	1.72477	11.06633	0.641
−4.5513	854.00	−9.67162	−2.56019	5430	1.87529	10.90763	0.608
−4.5018	800.00	−9.45556	−2.37263	5090	2.06296	10.73807	0.563
−4.4516	750.00	−9.24918	−2.18843	4840	2.24748	10.67806	0.520
−4.3828	700.00	−9.03754	−1.99525	4640	2.44075	10.71282	0.474
−4.2996	660.00	−8.86487	−1.83535	4510	2.60097	10.80808	0.439
−4.1540	615.00	−8.67305	−1.65092	4435	2.78547	10.96213	0.406
−3.8814	560.00	−8.44129	−1.42274	4400	3.01368	11.16643	0.375
−3.6627	525.00	−8.29662	−1.27720	4410	3.15957	11.30016	0.361
−3.4225	490.00	−8.15397	−1.13218	4435	3.30471	11.43425	0.350
−3.1354	450.00	−7.99439	−0.96778	4485	3.46909	11.58782	0.342
−2.7757	400.00	−7.80217	−0.76574	4590	3.67117	11.78061	0.338
−2.4230	350.00	−7.61529	−0.56848	4700	3.86847	11.97021	0.341
−2.0774	300.00	−7.43215	−0.37561	4805	4.06108	12.15625	0.367
−1.7383	250.00	−7.25344	−0.18709	4907	4.24895	12.33885	0.492
−1.4052	200.00	−7.07972	−0.00292	5010	4.43169	12.51957	0.688
−1.2415	175.00	−6.99654	0.08743	5080	4.52101	12.61300	0.792
−1.0801	150.00	−6.91614	0.17609	5165	4.60853	12.71029	0.900
−0.9208	125.00	−6.84103	0.26269	5288	4.69390	12.81928	1.023
−0.7625	100.00	−6.76981	0.34694	5431	4.77663	12.94191	1.153
−0.6012	75.00	−6.70377	0.42862	5607	4.85649	13.09096	1.286
−0.4302	50.00	−6.64397	0.50691	5826	4.93298	13.28081	1.434
−0.3182	35.00	−6.61297	0.55230	6006	4.97722	13.43600	1.522
−0.1933	20.00	−6.58620	0.59594	6231	5.01995	13.62921	1.601
−0.1007	10.00	−6.57009	0.62408	6397	5.04766	13.77034	1.651
0.0000	0.00	−6.55549	0.65147	6583	5.07482	13.92412	1.696
0.1092	−10.00	−6.54257	0.67806	6780	5.10072	14.08135	1.763
0.2274	−20.00	−6.53298	0.70372	7020	5.12581	14.26198	1.835
0.3555	−30.00	−6.52506	0.72843	7280	5.14953	14.44623	1.912
0.4940	−40.00	−6.52042	0.75213	7590	5.17289	14.64982	1.986
0.6415	−50.00	−6.51542	0.77481	7900	5.19590	14.83948	2.000
0.7944	−60.00	−6.51117	0.79664	8220	5.21854	15.02119	2.000
0.9499	−70.00	−6.50766	0.81757	8540	5.24005	15.18949	2.000
1.1048	−80.00	−6.50432	0.83771	8850	5.26079	15.34163	2.000
1.2548	−90.00	−6.49949	0.85715	9120	5.28081	15.46672	2.000
1.3978	−100.00	−6.49485	0.87593	9380	5.29994	15.58070	2.000

Table 6. VAL C7 semi-empirical non-LTE model of the solar **chromosphere** and transition region, adapted from [08Avr].

$\log \tau_{500}$	height [km]	$\log \rho$ [g cm^{-3}]	$\log m$ [g cm^{-2}]	T [K]	$\log P_{\rm gas}$ [dyn cm^{-2}]	$\log N_e$ [cm^{-3}]	$V_{\rm tur}$ [km s^{-1}]
−6.0449	2178.74	−14.12228	−5.41828	81220	−1.08307	9.58229	24.150
−6.0445	2175.28	−14.09648	−5.41794	76330	−1.08497	9.60681	23.670
−6.0440	2172.32	−14.07114	−5.41760	71810	−1.08677	9.63083	23.200
−6.0437	2169.99	−14.04847	−5.41737	68000	−1.08836	9.65244	22.780
−6.0434	2167.69	−14.02296	−5.41714	63950	−1.09012	9.67679	22.300
−6.0431	2166.03	−14.00187	−5.41703	60790	−1.09146	9.69697	21.900
−6.0429	2164.56	−13.98088	−5.41680	57790	−1.09275	9.71717	21.500
−6.0427	2163.29	−13.96019	−5.41669	55020	−1.09399	9.73687	21.110
−6.0425	2162.29	−13.94195	−5.41657	52690	−1.09501	9.75427	20.770
−6.0423	2161.26	−13.92082	−5.41646	50140	−1.09615	9.77423	20.370
−6.0422	2160.63	−13.90693	−5.41635	48490	−1.09686	9.78774	20.100
−6.0421	2160.01	−13.89177	−5.41623	46800	−1.09756	9.80202	19.810
−6.0419	2159.42	−13.87615	−5.41612	45140	−1.09827	9.81657	19.520
−6.0418	2158.84	−13.85918	−5.41601	43400	−1.09892	9.83251	19.200
−6.0417	2158.21	−13.83953	−5.41601	41450	−1.09969	9.85108	18.830
−6.0415	2157.57	−13.81730	−5.41589	39400	−1.10034	9.87175	18.410
−6.0413	2156.82	−13.78835	−5.41567	36870	−1.10106	9.89878	17.860
−6.0411	2156.16	−13.75970	−5.41556	34580	−1.10133	9.92536	17.300
−6.0410	2155.50	−13.72862	−5.41544	32260	−1.10149	9.95424	16.720
−6.0408	2154.73	−13.68846	−5.41533	29500	−1.10182	9.99127	15.990
−6.0405	2154.07	−13.65092	−5.41510	27130	−1.10210	10.02612	15.340
−6.0403	2153.48	−13.61672	−5.41499	25120	−1.10265	10.05767	14.790
−6.0401	2152.87	−13.57988	−5.41476	23100	−1.10347	10.09167	14.230
−6.0398	2152.03	−13.52739	−5.41454	20510	−1.10474	10.14019	13.460
−6.0393	2151.16	−13.47327	−5.41420	18140	−1.10613	10.18977	12.730
−6.0388	2150.12	−13.41005	−5.41375	15760	−1.10791	10.24527	11.930
−6.0379	2148.65	−13.32790	−5.41308	13200	−1.11092	10.31048	10.990
−6.0368	2147.05	−13.23837	−5.41218	10980	−1.12177	10.35641	10.280
−6.0355	2145.16	−13.12773	−5.41072	9115	−1.13501	10.36624	9.429
−6.0330	2141.93	−13.05301	−5.40782	7950	−1.14098	10.38561	8.874
−6.0299	2138.00	−13.00731	−5.40373	7248	−1.14104	10.41597	8.541
−6.0282	2136.00	−12.98885	−5.40154	6992	−1.14014	10.42878	8.407
−6.0265	2134.00	−12.97840	−5.39924	6870	−1.13805	10.43759	8.334
−6.0248	2132.00	−12.97143	−5.39696	6800	−1.13549	10.44483	8.285
−6.0230	2130.00	−12.96698	−5.39469	6768	−1.13253	10.45071	8.253
−6.0194	2126.00	−12.96019	−5.38998	6740	−1.12645	10.46075	8.205
−6.0139	2120.00	−12.95117	−5.38300	6718	−1.11708	10.47451	8.140
−6.0047	2110.00	−12.93704	−5.37120	6706	−1.10133	10.49485	8.039
−5.9931	2098.00	−12.91901	−5.35694	6700	−1.08218	10.51720	7.908
−5.9784	2083.00	−12.89551	−5.33904	6694	−1.05814	10.54345	7.736
−5.9500	2055.00	−12.84986	−5.30478	6686	−1.01309	10.58883	7.410
−5.9169	2024.00	−12.79588	−5.26576	6680	−0.96297	10.63377	7.038
−5.8784	1989.00	−12.73259	−5.22004	6674	−0.90483	10.68314	6.623
−5.8292	1946.00	−12.65150	−5.16121	6667	−0.83209	10.74186	6.124
−5.7678	1894.00	−12.54837	−5.08582	6660	−0.74160	10.80889	5.547
−5.6767	1820.00	−12.39287	−4.96981	6652	−0.60642	10.90020	4.779
−5.5516	1722.00	−12.17373	−4.79970	6643	−0.41737	11.01030	3.941
−5.4168	1617.00	−11.91686	−4.59482	6633	−0.19661	11.09968	3.165

Table 7. VAL C7 semi-empirical non-LTE model of the solar transition region and corona, adapted from [08Avr].

$\log \tau_{500}$	height [km]	$\log \rho$ [g cm^{-3}]	$\log m$ [g cm^{-2}]	T [K]	$\log P_{\rm gas}$ [dyn cm^{-2}]	$\log N_e$ [cm^{-3}]	$V_{\rm tur}$ [km s^{-1}]
−10.0000	68084.40	−15.83595	−5.92959	1586000	−1.50321	7.87408	34.000
−6.8914	47009.30	−15.66615	−5.80911	1410000	−1.38437	8.04415	34.000
−6.6590	36079.50	−15.56114	−5.74041	1294000	−1.31677	8.14891	34.000
−6.4962	26676.60	−15.45407	−5.67572	1170000	−1.25360	8.25600	34.000
−6.4073	21133.10	−15.37882	−5.63414	1080000	−1.21318	8.33122	34.000
−6.3163	15392.00	−15.28425	−5.58687	963700	−1.16787	8.42586	34.000
−6.2546	11596.20	−15.20461	−5.55207	865000	−1.13519	8.50542	34.000
−6.2098	8974.24	−15.13442	−5.52549	778300	−1.11087	8.57565	34.000
−6.1805	7360.82	−15.07972	−5.50752	711700	−1.09501	8.63043	34.000
−6.1494	5762.83	−15.00979	−5.48785	629300	−1.07857	8.70027	34.000
−6.1326	4968.64	−14.96417	−5.47703	577400	−1.07022	8.74601	34.000
−6.1174	4295.86	−14.91542	−5.46712	524300	−1.06329	8.79484	34.000
−6.1040	3752.71	−14.86423	−5.45830	471600	−1.05814	8.84597	34.000
−6.0952	3424.99	−14.82420	−5.45247	432900	−1.05552	8.88576	34.000
−6.0868	3133.79	−14.77963	−5.44685	392000	−1.05394	8.93039	34.000
−6.0818	2970.76	−14.74836	−5.44346	365000	−1.05370	8.96166	34.000
−6.0776	2844.40	−14.71965	−5.44069	341300	−1.05404	8.99047	34.000
−6.0748	2761.49	−14.69767	−5.43878	324000	−1.05468	9.01241	34.000
−6.0721	2688.10	−14.67551	−5.43687	307300	−1.05562	9.03463	34.000
−6.0699	2628.32	−14.65522	−5.43545	292500	−1.05675	9.05500	34.000
−6.0679	2578.23	−14.63620	−5.43403	279000	−1.05804	9.07408	34.000
−6.0662	2535.47	−14.61708	−5.43286	266700	−1.05859	9.09307	33.740
−6.0644	2495.56	−14.59671	−5.43168	254400	−1.05879	9.11327	33.330
−6.0628	2457.90	−14.57512	−5.43051	241900	−1.05914	9.13481	32.900
−6.0609	2418.66	−14.54960	−5.42934	227800	−1.05968	9.16047	32.390
−6.0589	2378.19	−14.51913	−5.42794	212000	−1.06053	9.19089	31.780
−6.0572	2346.10	−14.49066	−5.42678	198100	−1.06143	9.21932	31.220
−6.0561	2325.78	−14.47019	−5.42597	188600	−1.06218	9.23980	30.810
−6.0551	2308.55	−14.45075	−5.42527	180100	−1.06293	9.25912	30.420
−6.0542	2294.37	−14.43309	−5.42470	172600	−1.06364	9.27692	30.070
−6.0535	2282.38	−14.41680	−5.42423	166000	−1.06439	9.29314	29.740
−6.0527	2269.69	−14.39783	−5.42366	158600	−1.06525	9.31197	29.370
−6.0519	2259.43	−14.38091	−5.42308	152300	−1.06606	9.32899	29.030
−6.0514	2251.64	−14.36694	−5.42274	147200	−1.06677	9.34282	28.750
−6.0508	2243.32	−14.35076	−5.42228	141600	−1.06758	9.35889	28.430
−6.0502	2235.29	−14.33367	−5.42193	135800	−1.06849	9.37603	28.090
−6.0496	2227.74	−14.31614	−5.42148	130200	−1.06956	9.39340	27.760
−6.0490	2220.04	−14.29636	−5.42102	124000	−1.07084	9.41296	27.390
−6.0484	2213.74	−14.27835	−5.42067	118700	−1.07201	9.43088	27.050
−6.0479	2207.66	−14.25916	−5.42033	113200	−1.07330	9.44979	26.700
−6.0474	2201.92	−14.23890	−5.41999	107800	−1.07469	9.46982	26.320
−6.0468	2196.52	−14.21760	−5.41965	102300	−1.07619	9.49066	25.920
−6.0463	2191.46	−14.19504	−5.41919	96860	−1.07779	9.51255	25.500
−6.0457	2186.08	−14.16775	−5.41885	90640	−1.07977	9.53895	24.990
−6.0453	2182.44	−14.14655	−5.41851	86120	−1.08134	9.55919	24.600

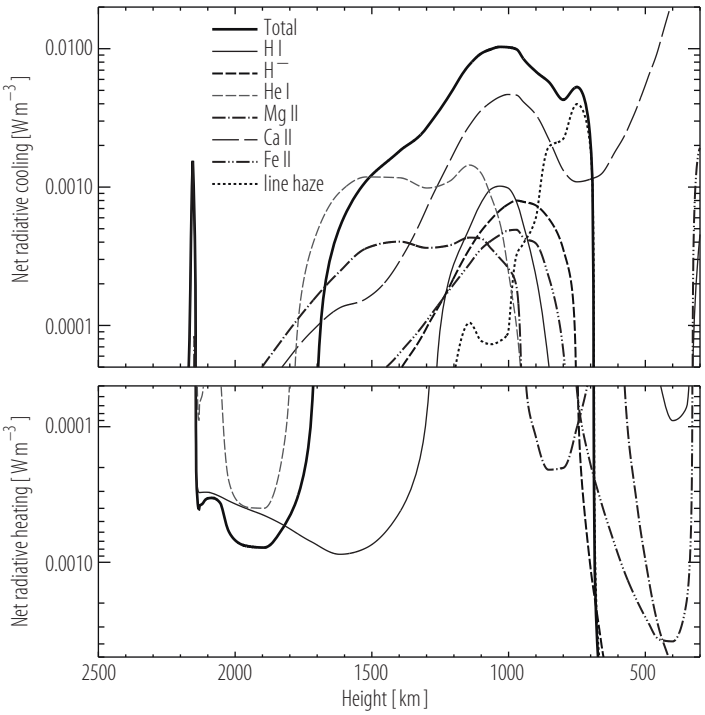

Fig. 4. Breakdown of chromospheric energy balance for model VAL C7 based on data provided by Avrett 2008 (priv. comm.). The upper (lower) panel shows the contribution of the most important chromospheric emission lines to the net radiative cooling (heating, on inverted scale) per unit volume as a function of geometrical height. *Total* (thick line) represents the sum of all contributions listed in Table 8. More detailed plots with cooling rates of individual species for the original VAL C model (and other members of the VAL family) may be found in [81Avr] and [85Avr].

presumably by the dissipation of acoustic and internal gravity waves. We note that the net radiative cooling rate was positive throughout the chromosphere in the original VAL C model (see [81Avr]), while it is *negative* in the upper chromosphere of VAL C7 (see Fig. 4), possibly indicating that the temperature gradient in the higher layers of the latter model is too shallow.

The chromospheric energy budget is summarized in Table 8, for both models VAL C [81Ver] and VAL C7 [08Avr]. According to the calculations by [81Avr], a lower limit of the resulting net radiative energy losses of the solar chromosphere is about 4.5 kW m^{-2}.

By design, the models of the VAL family provide a good fit to the UV spectrum of the average quiet Sun. They fail, however, to reproduce the strong lines of carbon monoxide (CO) in the infrared. When observed close to the solar limb, these lines show very low central intensities corresponding to radiation temperatures as low as 3700 K ([72Noy, 81Ayr2, 86Ayr, 89Ayr, 90Ayr]). Since the CO lines are now known to form in LTE [89Ayr, 00Uit], this implies a gas temperature of 3700 K in layers where the inner wings of the Ca H and K lines indicate a temperature of 4400 K. This dilemma probably indicates that the higher solar atmosphere cannot be represented properly by a single, plane-parallel stratification. A *thermal bifurcation* of solar atmosphere has been proposed by [81Ayr2] to explain the various observations, and a corresponding *two-component model* consisting of a cool component without chromospheric temperature rise (COOLC, filling factor 92.5%) and a hot component with chromospheric temperature rise (FLUXT, 7.5%) has been constructed by [86Ayr] to reproduce both the Ca H and K lines and the CO lines. Theoretically, the thermal bifurcation was argued to be the result of a thermal instability (CO cooling catastrophe, see [81Ayr1, 83Kne]).

Table 8. Integrated chromospheric emission of the VAL C model after [81Avr], and of the VAL C7 model computed by integration of the radiative cooling rates provided by Avrett 2008 (priv. comm.), shown in Fig. 4, over the height range where the total net cooling rate is positive (between 690 km and 1700 km).

Source		Radiative Flux [W m^{-2}]	
		VAL C	VAL C7
Ca II	H	490	202
Ca II	K	640	295
Ca II	866.2 nm	460	297
Ca II	849.8 nm	550	414
Ca II	854.2 nm	680	459
Ca II	other	–	0
Mg II	h	430	123
Mg II	k	520	96
Mg II	other	–	2
Fe II		–	162
H	Ly α	340	–5
H	other lines	–	791
H	bound-free	–	–895
H	free-free	–	74
H^-	bound-free	170	61
H^-	free-free	220	171
Line	haze	–	561
Other[a]		–	1683
Total		> 4500	4491

[a] includes the contribution of line and bound-free transitions of the following elements: He I, He II, C I, C II, O I, Na I, Mg I, Al I, Si I, Si II, S I, K I, Ca I, Fe I.

The most recent semi-empirical model of this type by [06Ayr] consists of 5 cool components (the so called COmosphere) plus one hot component representing the temperature stratification in the magnetic network, i.e. areas with localized non-radiative heating. This model is designed to reproduce both (i) the continuum intensities and their center-to-limb variation in the visible and near infrared, and (ii) the strength and center-limb behavior of the IR CO bands at λ 2.3 and 4.7μm. A comparison of the "best" COmosphere model by [06Ayr] with the VAL C7 model by [08Avr] is shown in Fig. 5. Tables of this and similar models can be found in [06Ayr].

Despite strong evidence to the contrary (e.g. [02Ayr]), there are still attempts to explain the complete body of observations, including the IR CO lines, by a single 1D temperature structure with a low temperature at the right place to reproduce the near-limb observations of the CO lines, and a sharp temperature increase to give enough intensity in the UV continua [07Fon].

A general weakness of the semi-empirical modeling approach is the large number of free parameters (like temperature and turbulent velocity as a function of height, in some cases non-gravitational forces) which are difficult to constrain in a unique way by the observations. In contrast, theoretical models allow to study the underlying physical processes with much fewer free parameters.

4.1.1.4.1.4 1D theoretical models of the solar photosphere

1-dimensional theoretical models are constructed to satisfy both the equation of hydrostatic equilibrium (Eq. 12) and an energy equation. In the simplest case, one assumes that the only energy

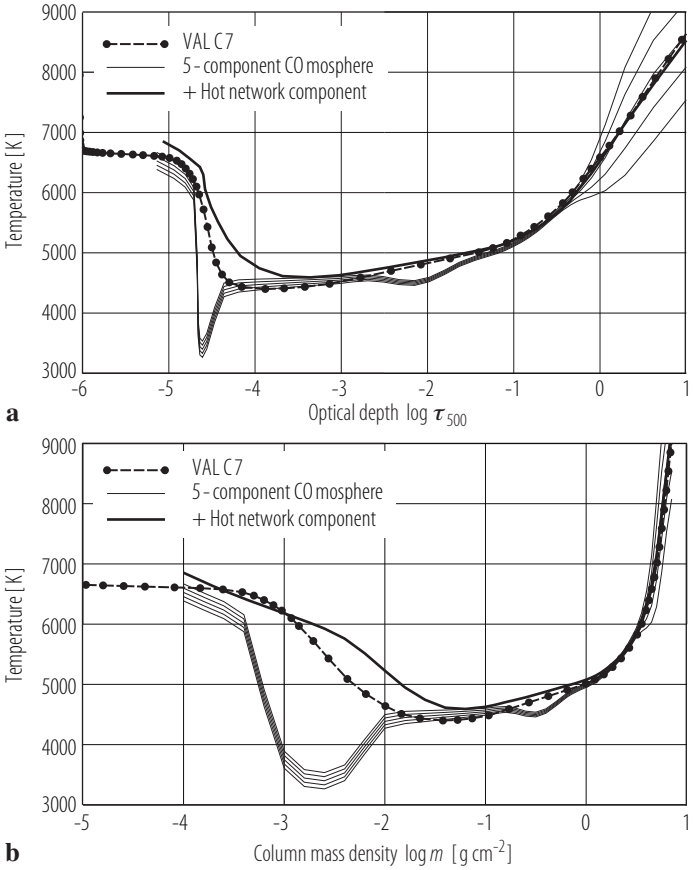

Fig. 5. Temperature structure of the semi-empirical "Double Dip" COmosphere model by [06Ayr] compared with that of model VAL C7 by [08Avr] on the optical depth scale τ_{500} (top) and on the mass scale m (bottom). The COmosphere model consists of 5 cool components covering 90% of the area (solid), plus a 10% contribution of a hot network component (thick solid). The deep outer temperature minimum is thought to be the result of efficient radiative cooling by the CO bands in the infrared. The smaller temperature dip in the mid-photosphere has no physical explanation yet and needs to be confirmed by further studies.

transport mechanism is radiation. The condition for *radiative equilibrium* (RE) is

$$\vec{F}_{\rm rad} \cdot \vec{e}_{\rm z} \equiv F_{\rm rad} = \sigma T_{\rm eff}^4 = \text{const.}\,, \quad \vec{e}_{\rm z} \text{ unit vector anti-parallel to gravity}\,, \tag{17}$$

i.e. the wavelength-integrated radiative energy flux is given by the solar effective temperature and is independent of height in the atmosphere. A fully non-LTE line-blanketed plane-parallel solar model atmosphere in radiative and hydrostatic equilibrium has been presented by [89And1], treating in great detail the non-LTE radiative transfer in millions of spectral lines. The resulting self-consistent thermal structure is shown in Fig. 6. In the chromospheric layers, very low temperatures down to $T \approx 2640$ K are found due to radiative cooling by carbon monoxide, corroborating the ideas by [81Ayr1].

Comparison of the RE model by [89And1] and the semi-empirical VAL C7 model by [08Avr] demonstrates that the real solar atmosphere is obviously not in RE. Rather, the chromospheric layers must be subject to non-radiative heating. This process was modeled in a seminal paper by [89And2], who introduced a prescribed mechanical energy flux, $F_{\rm mech}$, into the formalism of [89And1] to study the energy requirements for chromospheric heating. The energy equation now

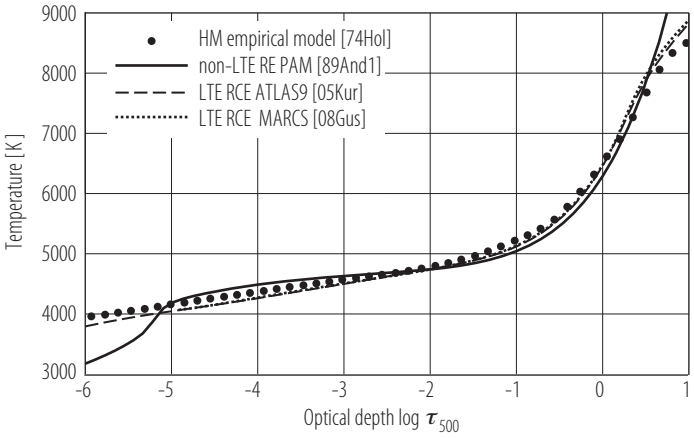

Fig. 6. Temperature structure of three different theoretical models of the solar atmosphere (solid and dashed lines) compared with the semi-empirical Holweger-Müller model (filled circles) on the $\tau_{500\,\mathrm{nm}}$ optical depth scale. The fully non-LTE line-blanketed radiative equilibrium model by [89And1] (solid) reaches very low temperatures, $T \approx 2640$ K, in the uppermost layers ($\log \tau_{\mathrm{Ross}} = -8.5$). The two LTE radiative-convective equilibrium solar models produced by the ATLAS9 and the MARCS code, respectively, are hardly distinguishable in this representation, except in the deepest layers where they diverge due to the different formalisms used to treat the convective energy transport.

reads

$$F_{\mathrm{rad}} + F_{\mathrm{mech}} = \mathrm{const.} \quad \text{or} \quad \vec{\nabla} \cdot \vec{F}_{\mathrm{rad}} + \vec{\nabla} \cdot \vec{F}_{\mathrm{mech}} = 0\,, \tag{18}$$

i.e. the local radiative losses are compensated by the dissipation of mechanical (wave) energy. According to the detailed investigation by [89And2], the mechanical heating required to sustain the thermal structure of the modified VAL C model by [86Mal] can be approximated as

$$-\frac{\vec{\nabla} \cdot \vec{F}_{\mathrm{mech}}}{\rho} \equiv Q_{\mathrm{mech}} \approx 4.55{\times}10^{9}[(m/0.003)^{5/3}{+}1]^{-3/2} \exp\{-m/0.0843\}\ [\mathrm{erg\,g^{-1}\,s^{-1}}]\,, \tag{19}$$

where m is the column mass density in [$\mathrm{g\,cm^{-2}}$]. This function is shown in Fig. 7 (in SI units), together with the corresponding mechanical energy flux

$$F_{\mathrm{mech}} = \int_0^m Q_{\mathrm{mech}}\,\mathrm{d}m\,. \tag{20}$$

Numerical integration of Eq. (19) gives a mechanical energy flux of 14 kW $\mathrm{m^{-2}}$ at the base of the chromosphere of VAL C type models. This is about 3 times larger than the value given by [81Avr] (4.5 kW $\mathrm{m^{-2}}$), presumably because the latter work does not treat the large number of lines of the iron group elements (mainly Fe II) in sufficient detail, which [89And2] claim to be the dominant source of radiation losses. As can be seen from Fig. 7, the heating rate per unit mass is essentially constant in the chromospheric temperature plateau, $Q_{\mathrm{mech}} \approx 4.5 \times 10^9$ erg $\mathrm{g^{-1}\ s^{-1}}$ or 450 kW $\mathrm{kg^{-1}}$. This plateau implies that $\vec{\nabla} \cdot \vec{F}_{\mathrm{mech}} \sim F_{\mathrm{mech}} \sim \rho$, which is the expected behavior of dissipating sound waves (see [89And3]).

More recently, a non-LTE line-blanketed solar photosphere model of even higher complexity was presented by [05Sho], including the energy transport by convection according to the mixing-length formalism (see below). The more rigorous method of treating the non-LTE problem incorporates many thousands of individual iron-group lines out of LTE, including about 20 000 Fe I and Fe II lines. The authors find that the non-LTE effects of Fe-group elements are much more important than the non-LTE effects of all the light metals combined. The theoretical $T(\tau)$ structure of their most

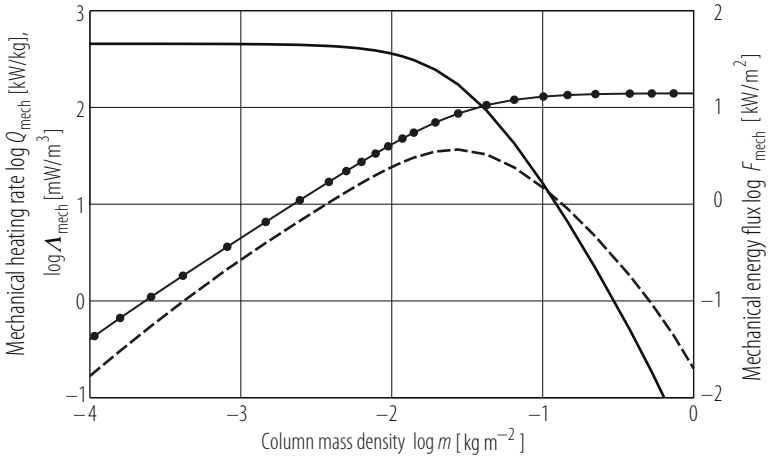

Fig. 7. Graphical representation of the mechanical heating rate per unit mass, $Q_{\rm mech}$ [kW kg^{-1}] (solid, left ordinate), and the mechanical energy flux $F_{\rm mech}$ [kW m^{-2}] (circles, right ordinate) as a function of column mass density m [kg m^{-2}] after [89And2]. The heating rate per unit volume, $\Lambda_{\rm mech} = \rho\, Q_{\rm mech}$ [mW m^{-3}] (dashed, left ordinate), has been computed from the density profile of the VAL C7 model.

realistic non-LTE model agrees to within 100 K with both the more approximate theoretical model of [89And1] and the LTE semi-empirical structure of the HM model [74Hol]. This agreement is a remarkable indication of the approximate non-LTE treatment developed by [89And1]. At the same time, it once again renders the HM model more reliable than the modified semi-empirical model proposed by [99Gre]. However, even the best theoretical solar model still predicts a significantly higher flux level in the near UV band than is observed. As demonstrated by [05Sho], the discrepancy is much too large to be due to errors in the model structure, suggesting that there may still be important UV opacity sources missing from the models (see however [09Sho], who point out that the variance among independent measurements of the solar irradiance in the near-UV is still too large to allow a definite conclusion about the significance of the UV opacity deficit).

Apart from the problem of computing the *radiative energy transport* in the presence of millions of spectral lines, another major difficulty in the construction of theoretical solar-type stellar atmosphere is a proper treatment of *convection*. In fact, a rigorous theory of the convective energy transport in stellar atmospheres is lacking due to the complexity of the underlying hydrodynamical processes. The "classical" 1-dimensional modeling of the solar interior and atmosphere still relies on a phenomenological approximation, the so called mixing-length theory (MLT, see e.g. [58Boe]), to calculate the convective energy flux, $\vec{F}_{\rm conv}$. The energy balance for such radiative-convective equilibrium models reads

$$F_{\rm rad} + F_{\rm conv} = \sigma T_{\rm eff}^4 \quad \text{or} \quad \vec{\nabla}\cdot\vec{F}_{\rm rad} + \vec{\nabla}\cdot\vec{F}_{\rm conv} = 0\,. \tag{21}$$

According to MLT, $\vec{F}_{\rm conv}$ can be calculated from local quantities (see e.g. [58Boe, 68Cox, 78Mih, h]):

$$F_{\rm conv} = \Lambda_{\rm MLT}\, f_2\, v_{\rm conv}\, \rho\, c_{\rm p}\, T\, (\nabla - \nabla_{\rm E})/H_{\rm p}\,, \tag{22}$$

where $v_{\rm conv}$ is the convective velocity given by

$$v_{\rm conv}^2 = \Lambda_{\rm MLT}^2\, f_1\, g\, \delta\, (\nabla - \nabla_{\rm E})/H_{\rm p}\,, \tag{23}$$

and the different temperature gradients ∇, $\nabla_{\rm E}$, and $\nabla_{\rm ad}$ (∇ stands for $\partial \ln T/\partial \ln P$) are related through the convective efficiency, Γ, via

$$\Gamma \equiv \frac{\nabla - \nabla_{\rm E}}{\nabla_{\rm E} - \nabla_{\rm ad}} = v_{\rm conv}\, \frac{\rho\, c_{\rm p}\, \tau_{\rm E}}{\sigma\, T^3}\, \frac{1}{f_3} \left(1 + \frac{f_4}{\tau_{\rm E}^2}\right)\,. \tag{24}$$

Here $\Lambda_{\rm MLT}$ is the mixing-length, a free parameter usually assumed to be proportional to the local pressure scale height, $\Lambda_{\rm MLT} = \alpha_{\rm MLT} H_{\rm p}$, where $\alpha_{\rm MLT}$ is the dimensionless mixing-length parameter of order unity. The geometrical constants f_1, f_2, f_3, f_4 are characteristic of different MLT formulations (see compilation in [99Lud]): in the original work by [58Boe] they are $f_1 = 1/8$, $f_2 = 1/2$, $f_3 = 24$, $f_4 = 0$; in the formulation by [78Mih] and in the ATLAS model atmospheres ([70Kur, 79Kur]) they are $f_1 = 1/8$, $f_2 = 1/2$, $f_3 = 16$, $f_4 = 2$; in the formulation by [65Hen] and in the MARCS model atmospheres ([75Gus, 03Gus, 08Gus]) they are $f_1 = 1/8$, $f_2 = 1/2$, $f_3 = 4\pi^2/24$, $f_4 = 4\pi^2/3$. The adiabatic temperature gradient $\nabla_{\rm ad}$ and $\delta \equiv -(\partial \ln \rho / \partial \ln T)_P$ are local thermodynamic quantities; $\tau_{\rm E} = \Lambda_{\rm MLT}\, \rho\, \overline{\kappa}$ is the optical thickness of the convective elements. All other symbols have their usual meaning.

The mean thermal structure of a convective stellar atmosphere can be found from the solution of Eqns. (21) to (24) for each level of the atmosphere. In optically thick layers ($\tau_{\rm E} \gg 1$), the problem reduces to the solution of a cubic equation. In the optically thin photospheric layers, an iterative temperature correction procedure is required to obtain the solution since the radiation field is no longer local.

Prominent examples of state-of-the-art LTE radiative-convective equilibrium models of the solar photosphere are (i) the Kurucz model computed with the ATLAS9 code as described in [05Kur], based on the NEW Opacity Distribution Functions (ODFs), adopting a chemical composition according to [05Asp] and $\alpha_{\rm MLT} = 1.25$, and (ii) the new MARCS solar model atmosphere as described in [08Gus] adopting $\alpha_{\rm MLT} = 1.5$ and a chemical composition according to [07Gre]. The temperature structures of these two models agree very closely, as shown in Fig. 6. Minor differences are found in the convective velocities (see Fig. 15). The complete models and corresponding synthetic flux distributions are available online from `http://wwwuser.oat.ts.astro.it/castelli/sun.html` and `http://www.marcs.astro.uu.se/`, respectively. ATLAS9 models based on alternative convection theories are discussed in [02Hei], and may be obtained from `http://www.univie.ac.at/nemo/`.

4.1.1.4.1.5 1D hydrodynamical simulations of the solar chromosphere

The effect of acoustic waves on the structure, dynamics, and energy balance of the solar chromosphere has been extensively studied by means of hydrodynamical simulations by Ulmschneider and coworkers already since the late 1970s (e.g. [77Ulm]), and by Carlsson & Stein ([92Car, 95Car, 97Car, 02Car1]). To make such calculations computationally tractable, the simulations were performed in 1D and magnetic fields were neglected.

The basic idea of these models is that acoustic shock waves are the main heating agent of the outer solar atmosphere, at least of the non-magnetic parts of the solar chromosphere (for a review on the mechanisms of chromospheric and coronal heating see e.g. [03Ulm]). Waves of relatively small amplitude arise quite naturally in the underlying convection zone that reaches into the low photosphere. When these waves travel upward, they experience a decrease in density, ρ, due to the gravitational stratification. This leads to an increase of the wave amplitude, $v_{\rm max}$, since the wave's energy flux, $F_{\rm wave} \propto \rho\, v_{\rm max}^2\, c_{\rm s}$, where $c_{\rm s}$ is the sound speed, is constant as long as the wave does not dissipate and is not damped by radiative energy exchange. The larger the wave amplitude becomes, the more important are nonlinear effects that make the wave peaks propagate faster than the valleys. Thus the peaks try to overtake the valleys until the wave 'breaks' and forms a quasi-discontinuous shock, which dissipates the wave energy by thermal conduction and viscosity in its steep shock front.

In the 1D hydrodynamical simulations, the waves are generated artificially be means of a piston located in the deep photosphere. In this way, the propagation and dissipation of monochromatic waves, as well as of waves with a prescribed energy spectrum, has been studied. A movie clip described in [07Ham] and available under `http://www.kis.uni-freiburg.de/media/KS06/` shows how a spectrum of waves moves through the solar atmosphere. The waves steepen into shocks that continue to grow with height; occasionally stronger shocks catch up and merge with weaker ones.

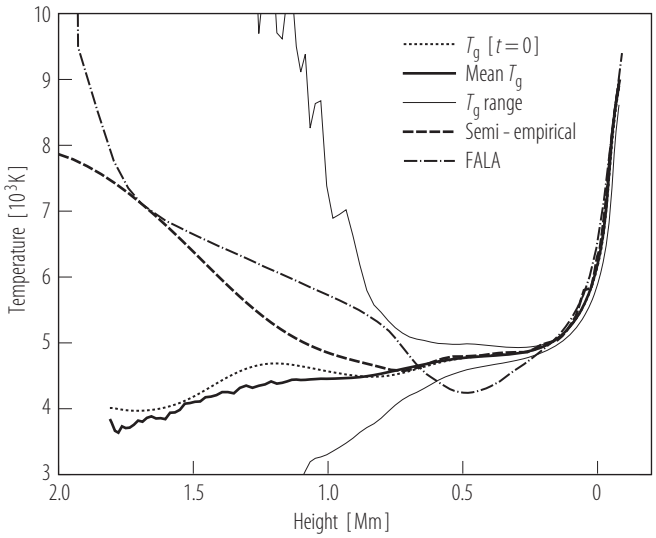

Fig. 8. Time average of the gas temperature in the dynamical simulation of [95Car] (thick solid) and the range of temperatures encountered in this simulation (thin solid), the semi-empirical model constructed to give the best fit to the time-averaged UV intensities calculated from the dynamical simulations (thick dashed), the initial model for the dynamical simulation (dotted), and the semi-empirical model FAL-A by [93Fon] (dot-dashed). The maximum temperatures are only reached in narrow shock spikes of short duration. The semi-empirical model giving the same intensities as the time-averaged emission of the dynamical simulation shows a chromospheric temperature rise, while the mean temperature in the simulation does not (reproduced from [95Car]).

The rather complex origin of the associated line emission is also illustrated in this animation for two wavelengths in the blue wing of Ca II K.

The emphasis of the modeling by Carlsson & Stein is on a very detailed description of the radiative processes and on the direct comparison with observations. The full non-LTE rate equations for the most important species in the energy balance (hydrogen, helium and calcium) are included, thus accounting for the effects of non-equilibrium ionization, excitation, and radiative energy exchange on fluid motions, and for the influence of Doppler shifts on the emitted radiation. To establish a direct link to observations, acoustic waves were injected at the bottom boundary with amplitudes and phases that matched observations of Doppler shifts in a photospheric iron line. These numerical simulations of the response of the chromosphere to acoustic waves close to the acoustic cut-off period of the atmosphere have been very successful in explaining the so called *Ca H and K Bright Grains* phenomenon, a characteristic variation of the line profiles of Ca II H and K that arises when strong acoustic shocks traverse the mid-chromosphere. As demonstrated by [97Car], their simulations reproduce the observed features to remarkable detail.

Another important result of this work is that the meaning of an 'average' temperature becomes questionable in the presence of large temperature fluctuations. As illustrated in Fig. 8, even though the time-averaged gas temperature of the dynamical simulation decreases monotonically with height, the corresponding hydrostatic model constructed to match the mean UV emission of the dynamical simulation must have a pronounced chromospheric temperature rise, comparable to that of the VAL-type empirical models of the solar chromosphere. This result demonstrates that it can be highly misleading to construct a mean static model to represent a situation that is actually strongly dynamic.

The simulations by [95Car] also confirmed that ionization/recombination timescales in hydrogen are longer than typical hydrodynamical timescales under solar chromospheric conditions, as pointed out before by [80Kne]. The hydrogen ionization balance is therefore out of equilibrium

and depends on the previous history of the atmosphere. Since the hydrogen ionization energy is an important part of the internal energy equation, this non-equilibrium ionization balance also has a very important effect on the energetics and temperature profile of the shocks ([92Car, 02Car1]).

Even though the 1D simulations described above explain reasonably well the dynamics of the low chromosphere (Ca Bright Grains), they fail to reproduce the lines and continua formed above about 0.8 Mm height which have much too low mean intensities in the models ([02Car2]). This failure can in principle have several possible reasons, including (i) the restriction to 1-dimensional geometry (cf. [05Ulm, 07Ram]), (ii) a severe underestimation of the contribution of high-frequency acoustic waves ($\nu > 20$ mHz, cf. [99Kal]), or (iii) the absence of magnetic fields in the simulations.

There is still no consensus about the main chromospheric heating agent. The common view that the non-magnetic chromosphere is heated by the dissipation of acoustic waves has recently been challenged by [05Fos1, 05Fos2, 06Fos]. They concluded that the small fluctuations in the UV continua (formed in the upper photosphere) as observed by the TRACE satellite permit only an acoustic energy flux that is at least an order of magnitude too small to balance the chromospheric energy losses. The cogency of this conclusion is however still under debate, as the spatial resolution of TRACE is only marginally sufficient to resolve the relevant scales ([07Wed1]). Therefore, it appears premature to declare the acoustic heating theory to be dead at this time, even though it has been argued that the role of internal gravity waves for heating the solar chromosphere has possibly been severely underestimated in the past ([08Str]).

Recent attempts to model the chromosphere in 3 dimensions, including magnetic fields, are addressed in Section 4.1.1.4.2.4.

4.1.1.4.2 3D structure and dynamics of the solar photosphere and chromosphere

Advanced time-dependent hydrodynamical simulations in 2 and 3 dimensions are becoming increasingly powerful tools for gaining basic insights into the complex phenomena revealed by modern observations of the solar photosphere and chromosphere at high spatial and temporal resolution.

4.1.1.4.2.1 Granulation

Images of the Sun taken with sufficient angular resolution reveal a characteristic cellular brightness pattern, the so-called *Solar Granulation*. The pattern was discovered already in 1801 by W. Herschel, who interpreted the pattern as being due to "hot clouds" floating over a cooler solar surface. The term "granules" was coined by R.W. Dawes (1864), contesting the description of J. Nasmyth (1862), who described them as having a shape similar to "willow leaves". The first successful photographs, taken by P.J. Janssen in 1877, ended the controversy in favor of Dawes' description. The correct physical interpretation of the phenomenon was first given by A. Unsöld (1930), who attributed the origin of the granulation to convective currents in the solar hydrogen ionization zone. (see [b] for a comprehensive historical introduction).

A modern high-resolution image of the quiet solar granulation, taken with the best ground-based solar telescope available to date, is shown in the left panel of Fig. 12. The typical brightness pattern covering the entire visible surface of the Sun is now understood to be the characteristic imprint of gas flows originating in the uppermost layers of the solar convection zone. The strong correlation between continuum intensity and Doppler velocity seen in 1D slit spectrograms (e.g. [03Pus]) or 2D Doppler maps (e.g. [01Hir]) after careful removal of the p-mode oscillations, clearly demonstrates that the bright 'granules' can be identified with hot rising gas flows, while the dark 'intergranular lanes' represent cool sinking gas.

The *intensity contrast*, $\delta I_{\rm rms}$, is an important measure of the granulation because it is directly related to the size of the temperature fluctuations. Given a time series of images, $I(x, y, t)$, the

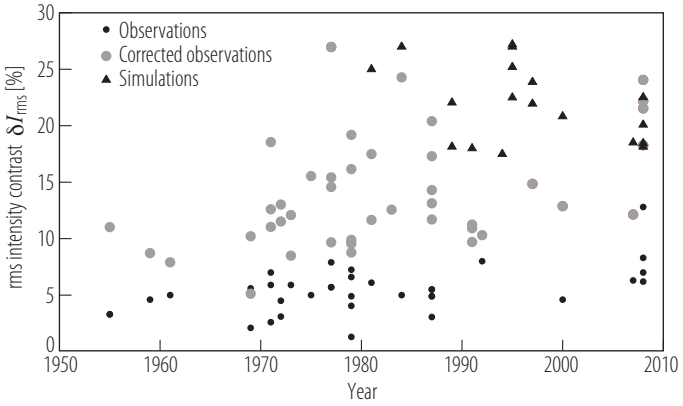

Fig. 9. Observed and synthetic rms intensity contrast $\delta I_{\rm rms}$ of the solar granulation at disk center, plotted as a function of publication year as listed in Tables 9 and 10. Points are raw data, measured at different wavelengths. Gray circles are values corrected for atmospheric and instrumental effects by the respective authors and then converted to continuum wavelength $\lambda\,500$ nm under the assumption $\delta I_{\rm rms} \propto 1/\lambda$. Triangles are predictions from hydrodynamical simulations, corrected for wavelength in the same way. Adapted from [08Kis].

(relative) rms intensity contrast of a single image is computed as

$$\delta I^2_{\rm rms}(t) = \frac{\langle (I(x,y,t) - I_0(t))^2 \rangle_{x,y}}{I_0^2(t)}\,, \quad I_0(t) \equiv \langle I(x,y,t) \rangle_{x,y}\,, \tag{25}$$

where $\langle\cdot\rangle_{x,y}$ indicates averaging over the 2-dimensional image. The mean intensity contrast is then obtained by quadratic averaging over the individual frames,

$$\delta I_{\rm rms} = \left[\langle \delta I^2_{\rm rms}(t) \rangle_t\right]^{1/2} \approx \frac{h\,c}{\lambda\,k\,T} \left(\frac{\delta T}{T}\right)_{\rm rms}\,. \tag{26}$$

The last approximation holds for optical wavelengths ($\lambda\,k\,T \ll h\,c$) where Wiens's law is valid.

The true value of $\delta I_{\rm rms}$, sometimes considered as the most important characteristic number associated with the solar granulation, has been debated for a long time. A selection of prominent measurements compiled from the literature is given in Table 9 and displayed graphically in Fig. 9. Many authors have tried to correct their observed values for the point spread function of their instrument and the degrading effects of the Earth's atmosphere at the moment of observation. The derived correction factors are often large. However, as is evident from the plot, the spread among the corrected values from the literature remains large. Apparently, the correction procedure is problematic. The other obvious conclusion is that the corrected measurements tend to lie significantly below the predictions of the hydrodynamical simulations discussed in detail in Section 4.1.1.4.2.2 (see Table 10 and Fig. 9). The reason for the endless debate about this discrepancy is that it is so difficult to precisely quantify the effects of scattered light – even if observations are acquired from space. Even in very recent work no consensus is reached. Using the Dunn Solar Telescope at Sac Peak with adaptive optics and employing speckle techniques, [07Uit] end up with a significant discrepancy between observations and simulations (14.1% versus 21.5% at $\lambda\,430.5$ nm). They suggest that the solution to this old dilemma is that the solar quiet photosphere is actually more strongly magnetic than commonly assumed, and hence should be compared with appropriate MHD simulations. On the other hand, [08Dan] claim a good correspondence between their simulations and observations from the Hinode space observatory, though they have to resort to assuming a somewhat ad hoc slight defocus of the instrument to achieve this agreement. Finally, [08Wed] have made an extensive investigation of the Hinode Point Spread Function and compared Hinode observations with their simulations ([09Wed2]). The rightmost points in Fig. 9 indicate that

Table 9. A selection of disk-center **rms intensity contrast measurements** of the solar granulation. Adapted from [00San].

Authors	λ [nm]	$\delta I_{\rm rms}$ [%] raw	corr.[a]	Remarks	Ref.
Frenkiel & Schwarzschild (1955)	580.0	3.3	–	Mt. Wilson photograph	[55Ube]
Uberoi (1955)	580.0	3.3	9.5	Mt. Wilson photograph	[55Fre]
Schwarzschild (1959)	545.0	4.6	8.0	Stratoscope I 1957	[59Sch]
Bahng & Schwarzschild (1961)	549.0	5.0	7.2	Stratoscope I 1959	[61Bah]
Beckers & Parnell (1969)	656.9	2.1	3.9	Sac Peak 30.5 cm	[69Bec]
Namba & Diemel (1969)	547.0	5.6	9.3	Stratoscope I 1959B/D	[69Nam]
Lévy (1971)	530.0	7.0	17.5	Pic-du-Midi, eclipse 66	[71Lev]
Mehltretter (1971)	552.0	5.9	10.0	JOSO, Sicily 70	[71Meh2]
Mehltretter (1971)	630.0	2.6	10 - 14	Capri 69	[71Meh1]
Canfield & Mehltretter (1973)	517.9	5.9	8.2	Sac Peak VTT 71	[73Can]
Deubner & Mattig (1975)	607.0	5.0	12.8	NVT, eclipse 73	[75Deu]
Edmonds & Hinkle (1977)	547.0	7.4 - 8.5	13.6 - 14.5	Stratoscope I 1959B	[77Edm]
Karpinsky & Mekhanikov (1977)	465.0	–	29	SSSO 1970	[77Kar]
Keil (1977)	552.0	5.7	13.2	Sac Peak VTT	[77Kei]
Wittmann & Mehltretter(1977)	556.0	5.7	8.7	Spektrostratoskop 75	[77Wit]
Ricort & Aime (1979)	505.0	1.3 - 7.25	16 - 19	Sac Peak 75	[79Ric]
Schmidt et al. (1979)	422.0	4.9	10.4	NVT, eclipse 76	[79Sch]
Schmidt et al. (1979)	556.0	4.05	8.6	Spektrostratoskop 75	[79Sch]
Wittmann (1979)	556.0	6.6	8.9	Spektrostratoskop 75	[79Wit]
Ricort et al. (1981)	530.0	–	16.5	Capri, eclipse 76	[81Ric]
Schmidt et al. (1981)	550.0	6.1	10.6	NVT, Izãna 79	[81Sch]
Durrant et al. (1983)	556.0	–	11.3	Spektrostratoskop 75	[83Dur]
Nordlund (1984)	607.0	5.0	20.0	re-evaluation of [75Deu]	[84Nor2]
v. d. Lühe & Dunn (1987)	517.0	3.06	11.7 - 13.7	Sac Peak, RCA CCD	[87Lue]
Collados & Vázquez (1987)	500.0	4.9 - 5.5	11.7 - 20.4	NVT, eclipse 84	[87Col]
Keller & Koutchmy (1991)	445.1	–	10.9	Sac Peak VTT	
Keller & Koutchmy (1991)	525.6	–	10.7	photographic	
Keller & Koutchmy (1991)	606.9	–	9.0	plates	[91Kel]
Rodriguez Hidalgo (1992)	468.6	8.0	11 - 12.5	SVST 1988	[92Rod]
Wilken et al. (1997)	550.0	–	13.5	VTT, speckle reconst.	[97Wil]
Sanchez Cuberes	670.8	4.6	9.6	SVST, during	[00San]
et al. (2000)				partial eclipse 94	[07Uit]
Uitenbroek et al. (2007)	430.5	5.0 - 7.5	14.1	DST with AO	[07Uit]
Danilovic et al. (2008)	630.0	7.0	14 - 15	*Hinode* SOT/SP	[08Dan]
Wedemeyer-Böhm	450.5	12.8	26.7	*Hinode* SOT/BFI	
and	555.1	8.3	19.4	*Hinode* SOT/BFI	
Rouppe van der Voort (2009)	668.3	6.2	16.6	*Hinode* SOT/BFI	[09Wed2]

[a] corr.: corrected for atmospheric and instrumental degradation.

finally convergence between simulations and observations seems to be achieved, near $\delta I_{\rm rms} \approx 20\%$ at $\lambda\,500$ nm. This value corresponds to $\delta T_{\rm rms} \approx \pm 250$ K (on the surface where $\tau_{500} = 1$) according to Eq. (26), in agreement with the value given in Table 12, column 5.

The observed center-to-limb variation $\delta I_{\rm rms}(\mu)$ is also analyzed in [09Wed2] and found to be in gratifying agreement with their simulation results. Note, however, that even for the space-borne SOT on-board Hinode the required correction factors are still large (final entries in Table 9).

The intensity distributions measured by [09Wed2] from selected images of the quiet solar photosphere near disk-center are displayed in Fig. 10 before and after correction for three different continuum bands, centered on $\lambda\lambda$ 450.5 nm (dashed), 555.1 nm (solid), and 668.4 nm (dotted),

Table 10. Theoretical predictions of the rms intensity contrast at disk-center from hydrodynamical simulations of the solar granulation.

Authors	λ [nm]	$\delta I_{\rm rms}$ [%] raw	Remarks	Ref.
Dravins et al. (1981)	500.0	20.0 - 30.0	3D anelastic	[81Dra]
Nordlund (1984)	600.0	20.0 - 25.0	3D anelastic	[84Nor2]
Lites at al. (1989)	630.0	14.4 - 17.5	3D compressible	[89Lit]
Steffen & Freytag (1991)	500.0	16.0 - 20.0	2D compressible	[91Ste]
Atroshchenko & Gadun (1994)	500.0	16.0 - 19.0	3D compressible	[94Atr]
Gadun & Vorob'yov (1995)	500.0	27.0	2D compressible	[95Gad]
Gadun et al. (1997)	491.2	24.3	2D compressible	[97Gad]
Asplund et al. (2000)	620.0	16.8	3D compressible	[00Asp1]
Uitenbroek et al. (2007)	430.5	21.5	3D MHD, G-band	[07Uit]
Danilovic et al. (2008)	630.0	14.4	3D MHD	[08Dan]
Wedemeyer-Böhm	450.5	25.0	3D RHD	
and	555.1	18.1	3D RHD	
Rouppe van der Voort (2009)	668.3	13.8	3D RHD	[09Wed2]

respectively. It is obvious that image degradation due to the instrument (diffraction and stray light) strongly influences the width and even the shape of the derived intensity distributions.

Information about the spatial distribution of the intensity fluctuations is provided by their *power spectrum*. The 1-dimensional power spectrum can be obtained from 1D scans of the 2D intensity field $I(x, y)$, e.g. along the slit of a spectrograph of length L. Defining the relative fluctuation as $f(x, y) = I(x, y)/I_0 - 1$, where $I_0 = \langle I(x, y)\rangle_{x,y}$, the 1D Fourier Transform of f is given by

$$F(k_x, y) = \int_0^L f(x, y)\, \exp(-\mathrm{i}\, k_x\, x)\, \mathrm{d}x \tag{27}$$

such that

$$f(x, y) = \frac{1}{2\,\pi} \int_{-\infty}^{\infty} F(k_x, y)\, \exp(+\mathrm{i}\, k_x\, x)\, \mathrm{d}k_x\,. \tag{28}$$

The 1D power spectrum is then defined as

$$P_1(k_x) = \frac{1}{2\pi\, L}\, \left\langle F^*(k_x, y) \cdot F(k_x, y)\right\rangle_y\,, \tag{29}$$

and by virtue of Parseval's theorem we have

$$\left\langle f(x, y)^2\right\rangle_{x,y} = \int_{-\infty}^{\infty} P_1(k_x)\, \mathrm{d}k_x = \delta I_{\rm rms}^2\,. \tag{30}$$

The 2D Fourier Transform of f can be computed directly from the 2D image of size L_x, L_y as

$$F(k_x, k_y) = \int_0^{L_x} \int_0^{L_y} f(x, y)\, \exp\left\{-\mathrm{i}\,(k_x\, x + k_y\, y)\right\}\, \mathrm{d}x\, \mathrm{d}y \tag{31}$$

such that

$$f(x, y) = \left(\frac{1}{2\,\pi}\right)^2 \int_{-\infty}^{\infty} \int_{-\infty}^{\infty} F(k_x, k_y)\, \exp\left\{+\mathrm{i}\,(k_x\, x + k_y\, y)\right\}\, \mathrm{d}k_x\, \mathrm{d}k_y\,. \tag{32}$$

The 2D power spectrum is then defined as

$$P_2(k_x, k_y) = \frac{1}{2\pi\, L_x}\, \frac{1}{2\pi\, L_y}\, F^*(k_x, k_y) \cdot F(k_x, k_y)\,. \tag{33}$$

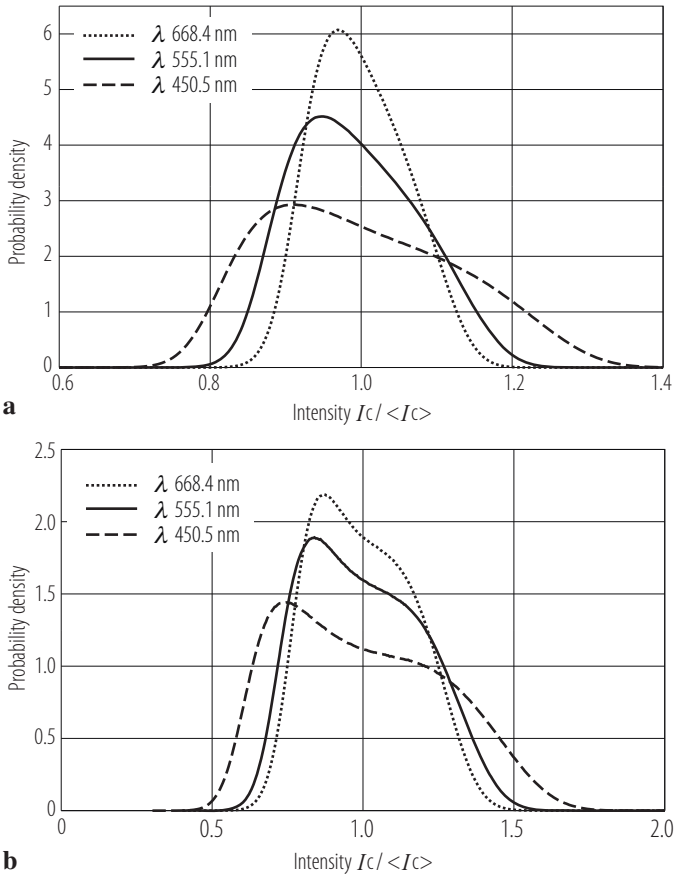

Fig. 10. Intensity histograms derived from selected images of the quiet solar photosphere near disk-center, taken with the Broadband Filter Instrument (BFI) of the Solar Optical Telescope (SOT) on-board the *Hinode* satellite. The three curves in each panel refer to continuum bands centered on $\lambda\lambda\,450.5$ nm (dashed), 555.1 nm (solid), and 668.4 nm (dotted), respectively. **Top**: distribution of uncorrected intensities, **bottom**: corrected for instrumental degradation including stray light. Note the different scales of upper and lower panel. All Probability Density Functions are normalized to unit area in the plotted coordinates. Data from [09Wed2].

Changing coordinates to $k = \sqrt{k_x^2 + k_y^2}$ and $\phi = \tan^{-1}(k_y/k_x)$, we can define a 1-dimensional representation of the 2D power spectrum:

$$P_2(k) = \int_{\phi=0}^{2\,\pi} k\, P_2(k\,\cos\phi, k\,\sin\phi)\mathrm{d}\,\phi \tag{34}$$

such that

$$\left\langle f(x,y)^2 \right\rangle_{x,y} = \int_{-\infty}^{\infty}\int_{-\infty}^{\infty} P_2(k_x,k_y)\,\mathrm{d}k_x\,\mathrm{d}k_y = \int_0^{\infty} P_2(k)\,\mathrm{d}k = \delta I_{\mathrm{rms}}^2\,. \tag{35}$$

If $P_2(k_x, k_y)$ is isotropic, i.e. depends only on k, then $P_2(k)$ can be related to $P_1(k)$ via an Abel transform (sometimes also called Uberoi transform, [53Ube]):

$$P_2(k) = -\frac{1}{2\,\pi}\int_k^{\infty} \frac{\mathrm{d}P_1(k')}{\mathrm{d}k'}\,\frac{1}{\sqrt{k'^2 - k^2}}\mathrm{d}k'\,. \tag{36}$$

If $P_1(k)$ follows a power law, $P_2(k)$ is also a power law with the same exponent.

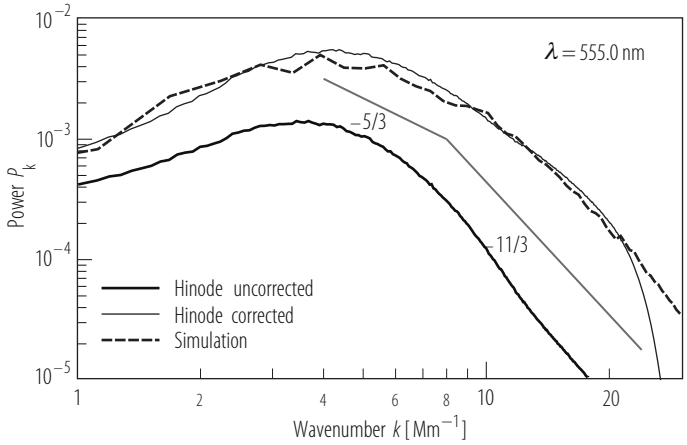

Fig. 11. 2D power spectra $P_2(k)$ derived from 14 images of the quiet solar photosphere near disk-center (each covering $224'' \times 112''$, with a resolution of 4096×2048 pixels), taken by the *Hinode* satellite in the green continuum at $\lambda\,555.1$ nm. In Fourier space, the correction for instrumental degradation (deconvolution) amounts to a k-dependent amplification of the uncorrected power spectrum (lower → upper solid curve). The cutoff due to the telescope's MTF is at $k \approx 40$ Mm^{-1}, but obviously the correction becomes unreliable already for $k > 20$ Mm^{-1}. The power spectrum obtained from 3 synthetic granulation images computed from the hydrodynamical models of [07Ste1] (dashed) is in close agreement with the results of the corrected observation.

The power spectra shown in Fig. 11 were computed according to Eq.(34). The power spectrum of the corrected observation agrees closely with that obtained from synthetic granulation images. No single characteristic slope is apparent, in conflict with claims in the literature (e.g. [93Esp, 97Hir]), where characteristic slopes of $-5/3$ and $-17/3$ have been identified and interpreted as evidence for the turbulent nature of the solar granulation. Other authors have argued that the slopes seen in the power spectra are simply determined by the sharpness of the edges in the granulation pattern and have nothing to do with turbulence ([97Nor]).

The *typical spatial scale* of the granulation pattern can be derived from the power spectrum and is usually defined as

$$\overline{k} = \int_0^{k_{\max}} k\,P_2(k)\mathrm{d}k \Big/ \int_0^{k_{\max}} P_2(k)\mathrm{d}k\,. \tag{37}$$

The result depends somewhat on the choice of $k_{\max}$: for the example shown in Fig. 11, we obtain $\overline{\Lambda} \equiv 2\,\pi/\overline{k} = 1.48$ Mm, 1.22 Mm, and 1.25 Mm for the uncorrected, corrected, and synthetic power spectrum, respectively, adopting $k_{\max} = 10$ Mm^{-1}, and $\overline{\Lambda} = 1.36$ Mm, 0.96 Mm, and 0.95 Mm when $k_{\max} = 20$ Mm^{-1}. These results may be compared with other methods used to define a characteristic size of the granulation, based on granule finding algorithms. The mean distance between the centers of adjacent granules, $\overline{d}$, has been found to be a well defined quantity; [86Rou1] obtained $\overline{d} = 1.76'' \sim 1.28$ Mm. The mean area of the granular cells A_c (defined as the area of granule plus associated intergranular lane) has been determined by [97Sch] and [00San], who find $A_c = 1.33$ Mm^2 and 1.36 Mm^2, respectively, corresponding to a mean cell diameter $D \approx 1.3$ Mm. Remarkably, virtually no granules with sizes $D > 2.2$ Mm are observed (e.g. [89Tit]).

The *fractal dimension* of granules, $D_f = 2\,\Delta \log P_g / \Delta \log A_g$ (P_g and A_g being the perimeter and the area of a granule, respectively) is evaluated in [86Rou1, 89Dar, 97Hir, 00San]. The authors largely agree that small granules are more regularly shaped than large ones. More specifically, the basic finding is that the fractal dimension changes quite abruptly from $D_f \approx 1.3$ for granules smaller than $\approx 1.4'' \sim 1000$ km, to $D_f \approx 2.1$ for the larger granules. Surprisingly, the fractal dimension of granular *cells* (granule plus associated dark lane) is independent of the cell size ($D_f \approx 1.2$, [97Hir]).

The *characteristic lifetime* of solar granules has recently been determined by [99Hir] applying different granule tracking methods to a 80 minute time series of high-resolution white-light images obtained at the Swedish Vacuum Solar Telescope (SVST). They obtain an exponential distribution of lifetimes, with a mean lifetime of $\tau \approx 5 \ldots 6$ minutes. This result is in basic agreement with earlier studies by [89Tit] who carried out an extensive analysis of Spacelab 2 SOUP movies and found $\tau \approx 5$ min from the lifetime distribution of individual granules followed by granule tracking, and $\tau \approx 5 \ldots 7$ minutes from the e-folding time of the temporal autocorrelation function of the quiet Sun. The results are shown to depend sensitively on the spatial resolution of the granulation images. A somewhat larger lifetime of $\tau \approx 7.5$ min is found by [01Mue], using a different approach. The concept of "families of fragmenting granules" is outlined by [03Rou], who find that long-lived families can exist for many *hours*, and may be related to meso-granules.

Studies of *solar cycle variations* of the solar granulation are notoriously difficult owing to the smallness of the effect and the high demands on the long-term stability of the observations. Based on the analysis of photographic images taken with the 50 cm refractor of the Pic-du-Midi observatory under excellent seeing conditions during the period 1978–1993, [07Mul] conclude that the granular intensity contrast varies very nearly in anti-phase with the solar cycle: the contrast is lowest during the periods of activity maximum. They find no evidence, however, for a concomitant variation of the granular scale, in contradiction to claims by [83Mac] and [86Rou2], who found a significant decrease of the mean size of the solar granules with increasing activity.

The *granular velocity field* can be measured via the Doppler effect. This requires spatially resolved spectroscopic observations that are much more difficult to obtain than granulation images. Due to the longer exposure times and the more complex optical setup necessary for spectroscopy, the spatial and temporal resolution of Doppler measurements is generally inferior to that of the intensity maps. Moreover, the interpretation of velocity data is complicated by the presence of solar oscillations which need to be separated from the granular motions. Another problem is that the origin of the Doppler signal cannot easily be related to a specific height level in the solar atmosphere, since a spectral line generally samples an extended range of atmospheric heights.

Despite these difficulties, the investigation of the *vertical structure* of the granular temperature and velocity fields is the subject of a large number of publications. One of the most robust results of such investigations is that the granular intensity fluctuations decrease rapidly with height, essentially disappearing near $z^* \approx 100$ km above the visible surface $\tau_{500} = 1$ (e.g. [99Kri]). Some authors find a weak reversal of the temperature contrast above z^* (e.g. [96Col, 03Pus]) which can be understood as the signature of overshoot. The granular vertical velocity field remains coherent over the whole photosphere, up to $z \approx 500$ km, but waves and turbulent motions appear to dominate the velocity fluctuations in the higher layers. Empirical models of typical solar granules have been published by [05Pus]. Readers interested in more details are referred to the papers by [91Kom, 95Esp, 00Kri, 01Hir, 06Nes] and the reference therein.

General overviews of the observed properties of the solar granulation have been given by [b, 89Mul, 99Mul, 5]. Although the observed statistical properties mentioned above are difficult to interprete in terms of the underlying physical processes, they are useful for a quantitative comparison with the results of the hydrodynamical simulations discussed in the following Section.

4.1.1.4.2.2 3D hydrodynamical simulations of the solar granulation

Convection, driven in the unstable sub-photospheric layers, has a strong impact on the dynamics and thermal structure of the overlying solar atmosphere: it influences not only the mean temperature stratification of the lower photosphere, but also generates substantial horizontal temperature inhomogeneities. Convective motions are not restricted to the convection zone proper (characterized by $\mathrm{d}s/\mathrm{d}\tau > 0$, where s and τ are specific entropy and optical depth, respectively) but in fact "overshoot" into the stably stratified layers above. Moreover, the stochastic convective motions have been shown to excite the solar p-modes (five-minute oscillations), and are a source of

acoustic energy flux, believed to contribute to the heating of the solar chromosphere (see Section 4.1.1.4.1.5).

A realistic treatment of convection and overshoot is beyond the capabilities of classical 1D hydrostatic model atmospheres, because (i) a self-consistent analytical convection theory is lacking, and (ii) the relevant hydrodynamical processes are intrinsically 3D and time-dependent. However, the differential equations governing the physics of stellar convection are well-known, namely the conservation equations of (magneto-)hydrodynamics, coupled with the equations of radiative transfer. The (ideal) MHD-equations can be written in conservative form as follows:

Continuity equation, describing the conservation of mass in a compressible fluid (ρ: gas density, $\vec{v}$: velocity field):

$$\frac{\partial \rho}{\partial t} + \vec{\nabla} \cdot (\rho \, \vec{v}) = 0 \tag{38}$$

Momentum equation, describing the conservation of the momentum of a magnetized fluid in an external gravitational potential Φ (P_g: gas pressure, P_rad: radiation pressure (negligible in the solar atmosphere), $\vec{B}$: magnetic field density):

$$\frac{\partial \rho \, \vec{v}}{\partial t} + \vec{\nabla} \cdot \left(\rho \, \vec{v} \, \vec{v} + \left[P_\mathrm{g} + P_\mathrm{rad} + \frac{\vec{B} \cdot \vec{B}}{2 \, \mu} \right] \underline{I} - \frac{\vec{B} \, \vec{B}}{\mu} \right) = -\rho \, \vec{\nabla} \, \Phi \;\; (= -\rho \, g \, \vec{e}_\mathrm{z}) \tag{39}$$

Energy equation, describing the conservation of the *total* energy per unit volume, E, in a magnetized, radiating fluid ($\vec{F}_\mathrm{rad}$: radiative energy flux):

$$\frac{\partial E}{\partial t} + \vec{\nabla} \cdot \left(\left[E + P_\mathrm{g} + \frac{\vec{B} \cdot \vec{B}}{2 \, \mu} \right] \vec{v} - \frac{1}{\mu} \, (\vec{v} \cdot \vec{B}) \, \vec{B} + \vec{F}_\mathrm{rad} \right) = 0 \tag{40}$$

Induction equation, describing the evolution of the magnetic field density due to fluid motions under the constraint that the field must remain solenoidal everywhere and at all times:

$$\frac{\partial \vec{B}}{\partial t} + \vec{\nabla} \cdot \left(\vec{B} \, \vec{v} - \vec{v} \, \vec{B} \right) = 0 \quad ; \quad \vec{\nabla} \cdot \vec{B} = 0 \tag{41}$$

Note the difference between the *dot product* of two vectors, which is a scalar, $\vec{A} \cdot \vec{B} = \sum_k A_k \, B_k$, and the *dyadic product* of two vectors, which is a tensor defined as $\vec{A} \, \vec{B} = \underline{C}$ with components $C_{i,j} = A_i \, B_j$. $\underline{I}$ is the 3×3 identity matrix. The total energy E is the sum of the *internal energy*, the *kinetic energy*, the *magnetic energy*, and the *potential energy*:

$$E = \rho \, \epsilon + \rho \, \frac{\vec{v} \cdot \vec{v}}{2} + \frac{\vec{B} \cdot \vec{B}}{2 \, \mu} + \rho \, \Phi \tag{42}$$

The magnetic permeability of the solar plasma is

$$\mu = \mu_0 = 4 \, \pi \cdot 10^{-7} \; [\mathrm{V \, s \, A^{-1} m^{-1}}] \tag{43}$$

The coupling between hydrodynamics and radiation is provided by the term $Q_\mathrm{rad} = \vec{\nabla} \cdot \vec{F}_\mathrm{rad}$ in the energy equation, Eq. (40). Given the hydrodynamic flow field, Q_rad must be obtained from the self-consistent solution of the non-local radiative transfer equation in 3 dimensions.

While the highly non-linear and non-local character of this problem precludes an adequate analytical treatment, the numerical integration of the system of partial differential equations constitutes an increasingly powerful approach to model stellar convection based on first principles. Using modern supercomputers, it is possible today to study in great detail the time-dependent properties of a radiating, partially ionized fluid under stellar conditions by means of 3-dimensional numerical simulations with realistic background physics (equation of state, radiative opacities) and

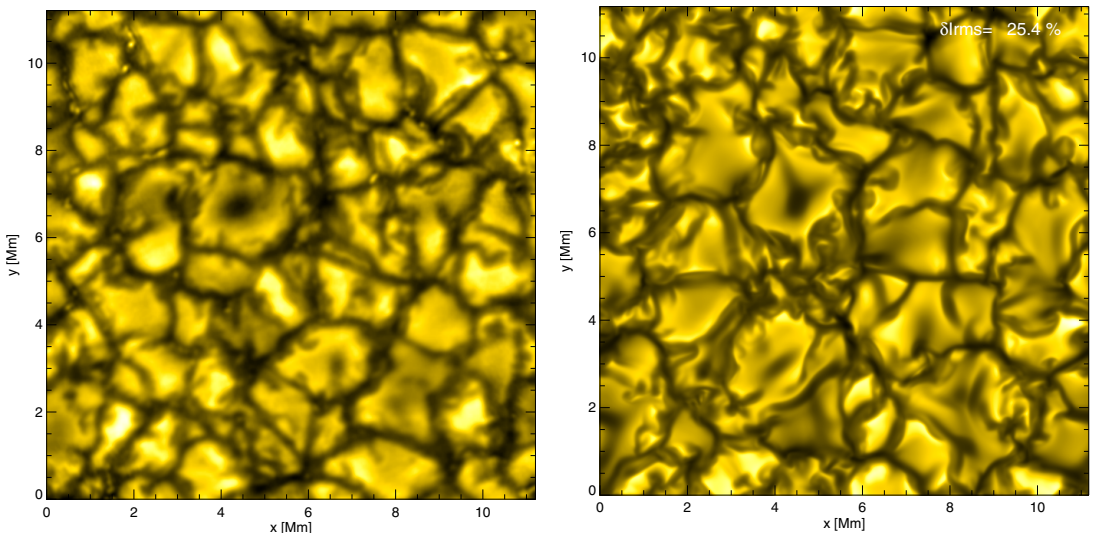

Fig. 12. (see color-picture part, page 613) Left: Quiet solar granulation as observed with the 1m Swedish Solar Telescope (courtesy Mats Carlsson 2004). **Right:** High-resolution CO^{5}BOLD simulation of solar surface convection on a $n_x \times n_y \times n_z = 400 \times 400 \times 165$ grid. Both images show the emergent continuum intensity (using identical scaling) at λ 436.4 nm in a field measuring $15'' \times 15''$ (11×11 Mm). Reproduced from [07Ste1].

considerable spatial resolution. It is important to realize that convection is driven by entropy fluctuations generated near the surface by radiative cooling. The deeper layers approach an adiabatic mean state in which ascending gas is nearly isentropic and uniform, and therefore have little direct influence on the small-scale granular flows at the surface. For this reason, it is possible to obtain physically consistent *ab initio* models of solar surface convection from "local box" simulations (with open boundaries) that cover only a small fraction of the geometrical depth of the entire convection zone. The resulting spatial structure and temporal scales of the flow develop naturally as a consequence of the underlying equations; they are not imposed on the simulations by external driving.

Just like "classical" stellar atmospheres, the *non-magnetic* hydrodynamical models are characterized by the average total energy flux per unit area and time (effective temperature), surface gravity, and chemical composition. But, in contrast to the mixing-length models, there is no longer any free parameter to adjust the efficiency of the convective energy transport. Similarly, the fudge parameters *micro-* and *macro-turbulence* that have to be introduced in 1D model atmospheres to match synthetic and observed line shapes, are replaced by the self-consistent hydrodynamical velocity field of the 3D simulations.

Radiation hydrodynamics. Hydrodynamical simulations of the solar granulation were pioneered by Nordlund & Stein beginning in the early 1980s (for details see e.g. [82Nor, 85Nor, 2]). A detailed discussion of the general properties of the solar surface layers as derived from their numerical simulations is given in [98Ste] and [00Ste], including a comparison with the observed properties of the solar granulation. More recently, other groups have presented models of similar sophistication (e.g. [04Wed, 05Voe, 07Ste1]). In all cases, the agreement between simulation and observation is remarkable, as illustrated by the examples given in Figs. 11, 12, and 13.

The role of convection in the excitation and damping of the solar p-mode oscillations is elaborated in [01Nor] and [01Ste]. It was demonstrated by [03Sam] that current numerical simulations of solar surface convection can be used successfully to predict solar p-mode excitation rates in agreement with observations. This approach has subsequently been extended to solar-type stars (e.g. [04Ste]).

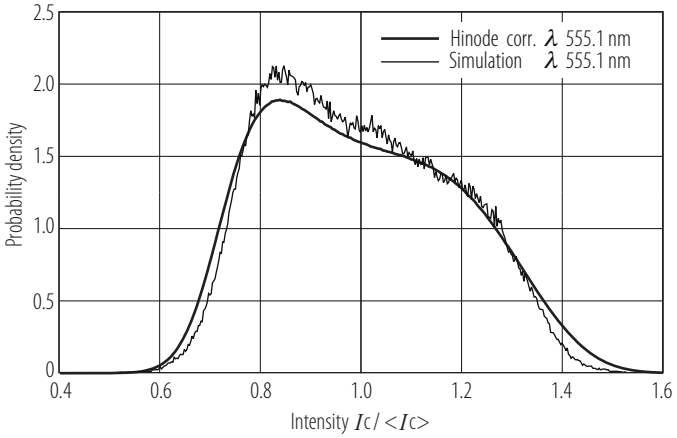

Fig. 13. Intensity probability density distribution derived from 14 selected images of the quiet solar photosphere near disk-center, taken by the *Hinode* satellite in the continuum at λ 555.1 nm, corrected for instrumental degradation (continuous line, cf. Fig. 10, right), compared with the intensity distribution obtained from 3 synthetic granulation images computed from the hydrodynamical model of [07Ste1] (noisy line). Remaining differences may indicate the presence of magnetic field concentrations in the observed images, which are ignored in this simulation.

From the beginning, the Nordlund & Stein models were also used to study the influence of solar convection on spectral line asymmetries and wavelength shifts (e.g. [81Dra, 82Dra, 84Nor1, 85Nor, 86Dra], and a recent review in [08Dra]). Subsequently, Asplund and coworkers used these 3D models for a spectroscopic re-determination of the chemical composition of the solar photosphere (e.g. [00Asp2, 00Asp3, 00Asp4]). The downward revision of the photospheric oxygen abundance advocated by [04Asp], together with the downward revision of the abundances of other important elements reported in [05Asp] (and references therein), has created serious problems for solar models to explain the helioseismic data (see [05Bah1, 05Bah2, 06Ant], or [08Bas] for details). An independent check of the results found by [04Asp] was recently presented by [08Caf], based on a thorough analysis of atomic oxygen lines with different 1D model atmospheres and their own state-of-the-art 3D model of the solar photosphere, computed with the radiation-hydrodynamics code CO^{5}BOLD ([02Fre, 04Wed]). Although they found a somewhat higher oxygen abundance by 0.1 dex, a serious discrepancy between the spectroscopically derived photospheric abundances and the metallicity inferred from helioseismology still remains.

Despite the impressive degree of realism exhibited by current 3D simulations of the solar granulation, it must be noted that these models still have their limitations. It is true that the free parameters needed in 1D computations to adjust the efficiency of the convective energy transport and the strength of the turbulent velocity field are no longer required in the framework of hydrodynamical models. However, the simulations are characterized by a set of numerical details, e.g. the numerical scheme used for solving the hydrodynamical equations, the spatial resolution of the numerical grid, and the formulation of boundary conditions. A particularly critical point is the treatment of radiative transfer: while the influence of millions of spectral lines on the radiative energy balance is taken into account in great detail in standard 1D models, it can be treated only approximately in the 3D simulations, typically using a few opacity bins. Finally, the (numerical) viscosity in the simulations is many orders of magnitude above realistic values, i.e. the Reynolds number of the simulations is far too small. Nonetheless, the hope is that the simulation results become essentially independent of the choice of these numerical parameters once a sufficiently high spatial, angular, and frequency resolution is achieved.

In view of the above mentioned imponderabilities, it is instructive to compare the mean structures obtained from two independent simulations. Figure 14 shows such a comparison between the 3D model used by [04Asp] (Table 11) and the 3D CO^{5}BOLD simulation employed by [08Caf]

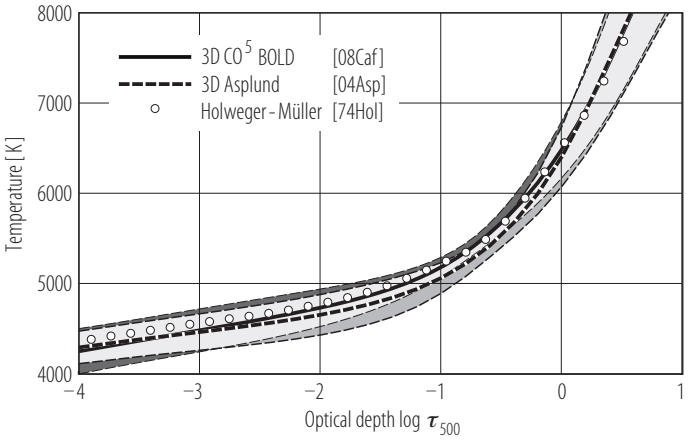

Fig. 14. Comparison of the mean temperature structures of the 3D model of the solar photosphere by [04Asp] (Table 11) with the 3D CO^{5}BOLD model by [08Caf] (Table 12). For both 3D models, the rms fluctuations (shaded areas) around the mean (thick lines) are indicated. The Holweger-Müller model [74Hol] (Table 3, open circles) is shown for reference.

Table 11. Temporally and spatially averaged atmospheric stratification of the 3D solar surface convection simulation by [04Asp]: temperature, density, gas pressure, electron pressure and vertical velocity (positive velocities upward) as well as their rms-scatter. The spatial averaging has been performed over surfaces of constant continuum optical depths at 500 nm. Note that the original 3D model extends significantly above and below the optical depths for which the mean structure has been interpolated to and tabulated.

τ_{500} (log)	T [K]	$\Delta T_{\rm rms}$ [K]	ρ [kg m^{-3}]	$\Delta\rho_{\rm rms}$ [kg m^{-3}]	$P_{\rm g}$ [Pa]	$\Delta P_{\rm g,rms}$ [Pa]	$P_{\rm e}$ [Pa]	$\Delta P_{\rm e,rms}$ [Pa]	$v_{\rm z}$ [km s^{-1}]	$\Delta v_{\rm z,rms}$ [km s^{-1}]
−5.00	4143	153	8.28(−7)	8.39(−8)	2.34(+1)	3.16(+0)	2.09(−3)	4.56(−4)	−0.06	1.53
−4.80	4169	161	1.09(−6)	1.16(−7)	3.10(+1)	4.40(+0)	2.73(−3)	6.39(−4)	−0.04	1.46
−4.60	4198	167	1.43(−6)	1.55(−7)	4.10(+1)	5.89(+0)	3.58(−3)	8.65(−4)	−0.03	1.37
−4.40	4230	172	1.88(−6)	1.99(−7)	5.41(+1)	7.54(+0)	4.69(−3)	1.14(−3)	−0.03	1.29
−4.20	4263	176	2.47(−6)	2.44(−7)	7.13(+1)	9.30(+0)	6.11(−3)	1.47(−3)	−0.03	1.22
−4.00	4297	180	3.21(−6)	2.90(−7)	9.34(+1)	1.12(+1)	7.94(−3)	1.88(−3)	−0.03	1.14
−3.80	4332	184	4.16(−6)	3.40(−7)	1.22(+2)	1.32(+1)	1.03(−2)	2.39(−3)	−0.03	1.07
−3.60	4368	188	5.36(−6)	3.99(−7)	1.58(+2)	1.55(+1)	1.32(−2)	3.03(−3)	−0.03	1.02
−3.40	4402	192	6.89(−6)	4.69(−7)	2.04(+2)	1.81(+1)	1.69(−2)	3.84(−3)	−0.03	0.96
−3.20	4435	197	8.82(−6)	5.56(−7)	2.63(+2)	2.11(+1)	2.16(−2)	4.88(−3)	−0.03	0.92
−3.00	4467	202	1.13(−5)	6.75(−7)	3.38(+2)	2.46(+1)	2.74(−2)	6.22(−3)	−0.04	0.89
−2.80	4500	207	1.44(−5)	8.38(−7)	4.33(+2)	2.89(+1)	3.48(−2)	7.93(−3)	−0.04	0.86
−2.60	4535	212	1.83(−5)	1.06(−6)	5.55(+2)	3.43(+1)	4.41(−2)	1.01(−2)	−0.04	0.84
−2.40	4571	217	2.32(−5)	1.35(−6)	7.10(+2)	4.11(+1)	5.59(−2)	1.30(−2)	−0.05	0.84
−2.20	4612	221	2.95(−5)	1.72(−6)	9.08(+2)	4.98(+1)	7.12(−2)	1.67(−2)	−0.06	0.85
−2.00	4658	224	3.75(−5)	2.16(−6)	1.16(+3)	6.05(+1)	9.12(−2)	2.14(−2)	−0.06	0.88
−1.80	4711	225	4.77(−5)	2.68(−6)	1.49(+3)	7.46(+1)	1.17(−1)	2.75(−2)	−0.07	0.93
−1.60	4773	221	6.05(−5)	3.27(−6)	1.92(+3)	9.27(+1)	1.53(−1)	3.50(−2)	−0.08	1.00
−1.40	4849	213	7.65(−5)	3.94(−6)	2.46(+3)	1.17(+2)	2.00(−1)	4.41(−2)	−0.09	1.10
−1.20	4944	196	9.61(−5)	4.83(−6)	3.14(+3)	1.52(+2)	2.67(−1)	5.44(−2)	−0.10	1.22
−1.00	5066	170	1.20(−4)	6.20(−6)	4.01(+3)	2.05(+2)	3.61(−1)	6.57(−2)	−0.10	1.38
−0.80	5221	141	1.47(−4)	8.30(−6)	5.08(+3)	2.83(+2)	5.02(−1)	8.04(−2)	−0.10	1.56
−0.60	5420	126	1.79(−4)	1.12(−5)	6.40(+3)	3.89(+2)	7.44(−1)	1.24(−1)	−0.09	1.76
−0.40	5676	154	2.13(−4)	1.57(−5)	7.97(+3)	5.27(+2)	1.27(+0)	3.48(−1)	−0.08	1.99
−0.20	6000	227	2.46(−4)	2.40(−5)	9.72(+3)	7.63(+2)	2.64(+0)	1.20(+0)	−0.06	2.22
0.00	6412	332	2.70(−4)	3.65(−5)	1.14(+4)	1.15(+3)	6.71(+0)	4.08(+0)	0.01	2.47
0.20	6919	481	2.82(−4)	5.17(−5)	1.28(+4)	1.66(+3)	1.98(+1)	1.47(+1)	0.13	2.71
0.40	7500	645	2.85(−4)	6.63(−5)	1.39(+4)	2.21(+3)	5.69(+1)	4.38(+1)	0.27	2.91
0.60	8084	759	2.83(−4)	7.78(−5)	1.49(+4)	2.74(+3)	1.33(+2)	9.44(+1)	0.39	3.05
0.80	8619	813	2.81(−4)	8.64(−5)	1.58(+4)	3.26(+3)	2.52(+2)	1.60(+2)	0.49	3.14
1.00	9086	817	2.79(−4)	9.30(−5)	1.67(+4)	3.77(+3)	4.08(+2)	2.30(+2)	0.56	3.19
1.20	9478	782	2.79(−4)	9.82(−5)	1.76(+4)	4.30(+3)	5.90(+2)	2.92(+2)	0.61	3.20
1.40	9797	719	2.82(−4)	1.02(−4)	1.86(+4)	4.83(+3)	7.82(+2)	3.36(+2)	0.64	3.18
1.60	10060	644	2.87(−4)	1.06(−4)	1.97(+4)	5.37(+3)	9.84(+2)	3.64(+2)	0.66	3.13
1.80	10290	573	2.96(−4)	1.08(−4)	2.09(+4)	5.89(+3)	1.21(+3)	3.95(+2)	0.67	3.06
2.00	10493	509	3.09(−4)	1.10(−4)	2.25(+4)	6.38(+3)	1.46(+3)	4.36(+2)	0.67	2.96

Table 12. Temporally and spatially averaged atmospheric stratification of the solar CO5BOLD model by [08Caf]. The spatial average was taken over surfaces of equal vertical Rosseland optical depths, the temporal average over 19 selected snapshots. The first three columns present the Rosseland optical depth, continuum optical depth at 500 nm, and the geometrical height scale (increasing outwards), respectively. The following columns present the mass density, gas pressure, electron pressure, and vertical velocity (positive velocities upward) as well as their rms-fluctuations. The original 3D model extends significantly above and below the optical depths for which the mean structure has been tabulated.

$\tau_{\rm ross}$ (log)	τ_{500} (log)	z [km]	T [K]	$\Delta T_{\rm rms}$ [K]	ρ [kg m^{-3}]	$\Delta\rho_{\rm rms}$ [kg m^{-3}]	$P_{\rm g}$ [Pa]	$\Delta P_{\rm g,rms}$ [Pa]	$P_{\rm e}$ [Pa]	$\Delta P_{\rm e,rms}$ [Pa]	$v_{\rm z}$ [km s^{-1}]	$\Delta v_{\rm z,rms}$ [km s^{-1}]
−5.00	−4.90	686	4061	305	9.62(−7)	1.75(−7)	2.48(+1)	3.86(+0)	2.19(−3)	9.26(−4)	−0.03	1.42
−4.80	−4.72	659	4094	285	1.26(−6)	2.00(−7)	3.28(+1)	4.29(+0)	2.84(−3)	1.02(−3)	−0.04	1.35
−4.60	−4.54	633	4131	269	1.64(−6)	2.33(−7)	4.29(+1)	4.88(+0)	3.68(−3)	1.15(−3)	−0.05	1.28
−4.40	−4.36	607	4171	256	2.10(−6)	2.75(−7)	5.58(+1)	5.66(+0)	4.77(−3)	1.34(−3)	−0.05	1.22
−4.20	−4.17	582	4213	247	2.69(−6)	3.28(−7)	7.22(+1)	6.67(+0)	6.16(−3)	1.60(−3)	−0.05	1.17
−4.00	−3.99	557	4257	242	3.44(−6)	3.97(−7)	9.31(+1)	7.96(+0)	7.95(−3)	1.95(−3)	−0.05	1.11
−3.80	−3.80	532	4301	239	4.38(−6)	4.86(−7)	1.20(+2)	9.60(+0)	1.02(−2)	2.41(−3)	−0.05	1.07
−3.60	−3.61	507	4345	239	5.57(−6)	6.03(−7)	1.54(+2)	1.17(+1)	1.32(−2)	3.02(−3)	−0.05	1.02
−3.40	−3.42	481	4389	239	7.08(−6)	7.55(−7)	1.98(+2)	1.43(+1)	1.69(−2)	3.81(−3)	−0.05	0.99
−3.20	−3.23	456	4433	239	9.00(−6)	9.50(−7)	2.54(+2)	1.77(+1)	2.17(−2)	4.84(−3)	−0.05	0.95
−3.00	−3.03	430	4478	240	1.14(−5)	1.19(−6)	3.25(+2)	2.19(+1)	2.78(−2)	6.14(−3)	−0.06	0.93
−2.80	−2.84	404	4522	239	1.45(−5)	1.49(−6)	4.16(+2)	2.70(+1)	3.57(−2)	7.78(−3)	−0.06	0.91
−2.60	−2.65	377	4568	238	1.83(−5)	1.84(−6)	5.33(+2)	3.30(+1)	4.57(−2)	9.81(−3)	−0.06	0.90
−2.40	−2.45	351	4615	235	2.32(−5)	2.23(−6)	6.81(+2)	3.99(+1)	5.85(−2)	1.23(−2)	−0.07	0.90
−2.20	−2.26	324	4664	229	2.93(−5)	2.66(−6)	8.71(+2)	4.77(+1)	7.50(−2)	1.53(−2)	−0.07	0.91
−2.00	−2.07	297	4717	222	3.70(−5)	3.12(−6)	1.11(+3)	5.66(+1)	9.63(−2)	1.89(−2)	−0.08	0.94
−1.80	−1.87	269	4775	211	4.66(−5)	3.60(−6)	1.42(+3)	6.70(+1)	1.24(−1)	2.30(−2)	−0.09	0.99
−1.60	−1.68	241	4840	197	5.84(−5)	4.10(−6)	1.80(+3)	8.02(+1)	1.60(−1)	2.76(−2)	−0.09	1.05
−1.40	−1.48	212	4916	179	7.30(−5)	4.64(−6)	2.29(+3)	9.85(+1)	2.08(−1)	3.27(−2)	−0.10	1.14
−1.20	−1.29	183	5006	158	9.08(−5)	5.35(−6)	2.90(+3)	1.26(+2)	2.72(−1)	3.84(−2)	−0.11	1.24
−1.00	−1.10	152	5118	134	1.12(−4)	6.40(−6)	3.67(+3)	1.69(+2)	3.62(−1)	4.51(−2)	−0.11	1.37
−0.80	−0.91	121	5257	113	1.38(−4)	7.95(−6)	4.62(+3)	2.32(+2)	4.94(−1)	5.57(−2)	−0.11	1.52
−0.60	−0.72	90	5430	106	1.67(−4)	1.02(−5)	5.78(+3)	3.18(+2)	7.07(−1)	8.78(−2)	−0.11	1.69
−0.40	−0.53	58	5645	128	1.98(−4)	1.34(−5)	7.15(+3)	4.32(+2)	1.11(+0)	2.17(−1)	−0.11	1.86
−0.20	−0.33	27	5908	180	2.30(−4)	1.86(−5)	8.66(+3)	5.85(+2)	1.99(+0)	6.51(−1)	−0.11	2.04
0.00	−0.14	0	6226	254	2.57(−4)	2.72(−5)	1.02(+4)	8.26(+2)	4.11(+0)	1.93(+0)	−0.08	2.24
0.20	0.06	−24	6605	343	2.76(−4)	3.95(−5)	1.16(+4)	1.22(+3)	9.38(+0)	5.43(+0)	−0.02	2.44
0.40	0.25	−44	7058	460	2.87(−4)	5.42(−5)	1.28(+4)	1.75(+3)	2.30(+1)	1.52(+1)	0.10	2.65
0.60	0.44	−60	7585	595	2.89(−4)	6.89(−5)	1.38(+4)	2.33(+3)	5.73(+1)	3.96(+1)	0.23	2.83
0.80	0.62	−74	8134	706	2.88(−4)	8.09(−5)	1.47(+4)	2.88(+3)	1.28(+2)	8.51(+1)	0.34	2.96
1.00	0.81	−85	8654	773	2.85(−4)	9.03(−5)	1.56(+4)	3.41(+3)	2.46(+2)	1.50(+2)	0.43	3.04
1.20	0.99	−96	9115	800	2.84(−4)	9.76(−5)	1.65(+4)	3.92(+3)	4.06(+2)	2.25(+2)	0.50	3.10
1.40	1.17	−107	9507	789	2.84(−4)	1.04(−4)	1.73(+4)	4.45(+3)	5.96(+2)	2.98(+2)	0.55	3.12
1.60	1.36	−119	9828	745	2.86(−4)	1.09(−4)	1.83(+4)	4.99(+3)	7.96(+2)	3.57(+2)	0.59	3.12
1.80	1.56	−132	10087	677	2.92(−4)	1.13(−4)	1.94(+4)	5.52(+3)	9.99(+2)	3.97(+2)	0.61	3.08
2.00	1.76	−148	10307	602	3.02(−4)	1.15(−4)	2.07(+4)	6.05(+3)	1.22(+3)	4.30(+2)	0.62	3.01

(Table 12), together with the semi-empirical HM model as a reference. In the low photospheric layers ($-0.7 < \log \tau_{500} < 0$), the average CO5BOLD stratification follows the HM model rather closely. As a consequence, the CO5BOLD model reproduces the observed solar center-to-limb variation in the continuum remarkably well ([09Lud]). As demonstrated in Fig. 15, the hydrodynamical velocity field found in the two simulations is in noteworthy agreement, but differs dramatically from the predictions of mixing-length theory, where the convective velocity vanishes in the stable photospheric layers.

It is not obvious which of the 3D models provides the better overall representation of the solar photosphere. Nonetheless, the differences seen in Fig. 14 provide an estimate of the systematic uncertainties that are present in the current generation of hydrodynamical solar atmospheres.

Magneto-convection. The purely hydrodynamical simulations described above provide essentially parameter-free *ab initio* models: the resulting mean flow is determined only by the prescribed

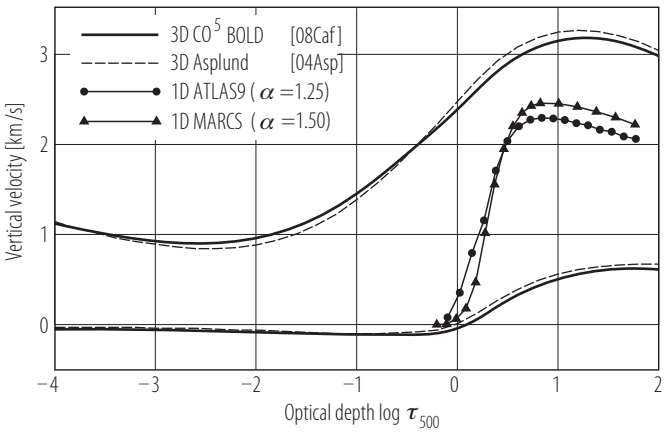

Fig. 15. Comparison of the mean vertical velocity, v_z (lower pair of curves) and the total root mean square vertical velocity, $v_{z,rms} = \sqrt{(\Delta v_{z,rms})^2 + v_z^2}$ (upper pair of curves) of the 3D model of the solar photosphere by [04Asp] (Table 11) with the results of the 3D CO5BOLD model by [08Caf] (Table 12). The convective velocity obtained from the ATLAS9 and MARCS LTE 1D radiative-convective equilibrium solar models (cf. Fig. 6) are shown as filled circles and triangles, respectively.

physical quantities T_{eff}, g, and the assumed chemical composition; it is largely independent of the formulation of the boundary conditions and details of the initial configuration. This is no longer true for the more complex simulations of solar *magneto-convection*. In this case, the presence of a magnetic field implies an extra degree of freedom, opening up a multitude of alternative choices in setting up the problem. The initial configuration of the magnetic field and the magnetic boundary conditions have to be designed for the particular problem under consideration. In many studies, the vertical magnetic field is prescribed to fix the mean magnetic flux at a given value, e.g. $\langle B_z \rangle \approx 200$ G to represent a solar plage region ([04Car, 05Voe]). More recently, another setup has been devised where a horizontal magnetic field of given strength is fed into the computational box through the open lower boundary ([06Ste1, 08Ste]). The solution obtained from this type of magneto-convection simulations describes the interaction of granular convection with an imposed external field (representing e.g. an active region, a pore, or a sunspot), and depends critically on the initial and boundary conditions adopted for the magnetic field. As a consequence, such "local box" models cannot make any predictions about the level of magnetic activity of the Sun.

There is mounting evidence that even the quiet solar photosphere is not field-free but rather permeated by small-scale, mixed polarity magnetic fields that show no significant variation with the solar activity cycle (see e.g. [04Tru]). It has been suggested that a considerable part of the quiet Sun magnetic fields may be produced by a self-excited turbulent dynamo operating in the near-surface layers of the Sun, even though the flow in these layers is not noticeably affected by rotation and thus exhibits no net helicity. The principle of such a non-helical surface dynamo has been demonstrated in incompressible, closed-box MHD simulations of thermal convection at high Rayleigh number by [99Cat, 03Cat], but it was unclear whether their results remain valid for the case of realistic solar granulation. The latter question was addressed by [07Voe]. who presented a first example of dynamo action in a realistic simulation of solar surface convection with an open lower boundary, indicating that the flow topology developing in strongly stratified, compressible, and non-helical surface convection without enforced recirculation is indeed capable of driving a turbulent local dynamo (see Fig. 16)

In principle, near-surface magneto-convection simulations could provide a self-consistent description of the local dynamo, including a prediction of its contribution to the mean magnetic flux of the quiet Sun. It must be noted, however, that the work by [07Voe] is only a first step in this direction, and their model is not yet suitable for a quantitative comparison with observations. This

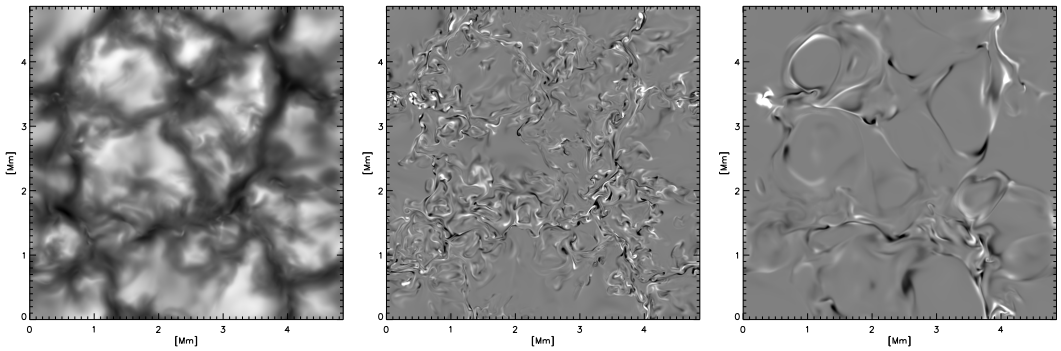

Fig. 16. Snapshot from the dynamo run by [07Voe] with $R_\mathrm{m} = 2600$, taken about 5 hours after introducing the seed field. The vertically emerging (bolometric) intensity (left) reveals the normal granulation pattern. The other panels show the vertical component of the magnetic field at two different heights. Near the visible surface ($\tau_\mathrm{R} = 1$, middle, grey scale saturating at ± 250 G), the magnetic field shows an intricate small-scale pattern with rapid polarity changes and an unsigned average flux density of $\langle |B| \rangle = 25.1$ G. About 300 km higher ($\tau_\mathrm{R} = 0.01$, right, grey scale saturating at ± 50 G), $\langle |B| \rangle$ has decreased to 3.2 G and the field distribution has become considerably smoother, roughly outlining the network of intergranular downflow lanes (darker areas on the left panel). Reproduced from [07Voe].

is because the simulation results depend critically on the magnetic Reynolds number, R_m as well as on the magnetic Prandtl number, Pr_m, i.e. on the achievable spatial resolution. The crucial question is whether the local dynamo can still operate in the limit of very small Pr_m, which is not (yet) accessible in the numerical simulations. Clearly, the dependence of the saturation level on R_m and Pr_m has to be investigated systematically through series of numerical experiments before reliable quantitative predictions are possible, for the Sun as well as for other solar-type stars.

4.1.1.4.2.3 Supergranulation and network

Mass conservation rules the horizontal scale of convection in a stratified atmosphere: the diameter of a cylindrical convection cell, D, is given by

$$D = 4\, H_\rho \, \frac{u}{v}\,, \tag{44}$$

where $H_\rho = -(\mathrm{d} \ln \rho / \mathrm{d}z)^{-1}$ is the local density scale height, u is the horizontal outflow velocity at the periphery of the cell, and v is the mean vertical (ascent) velocity (see e.g. [89Ste]). This simple relation may serve as guide to estimate the variation of the typical cell size with depth in the solar convection zone. Assuming that the ratio u/v is typically of order unity for the eddies dominating the energy transport (as in the granulation at the solar surface), and noting that H_ρ is roughly proportional to temperature and hence increases strongly with depth in the convection zone, Eq. (44) implies that consecutively larger scale motions dominate convection below the solar surface. This qualitative view is confirmed by supercomputer models, showing that the characteristic scale of convection increases systematically with depth in accord with the local pressure ($\approx$ density) scale height (e.g. [06Ste2]). It is important to realize that even though the surface layers cannot generate convection at scales much larger than a few times the local pressure scale height, they still feel the presence of larger scale flows being driven in deeper layers through their long-range pressure fields ([82Nor, 2]). The latter is associated with a weak surface velocity field which is predominantly horizontal, as can again be seen from Eq. (44), where now H_ρ is the density scale height at the surface, while D refers to the larger-than-granular scale of the subsurface flow. Since D is much larger than H_ρ, u must be much larger than v. Consequently, these larger

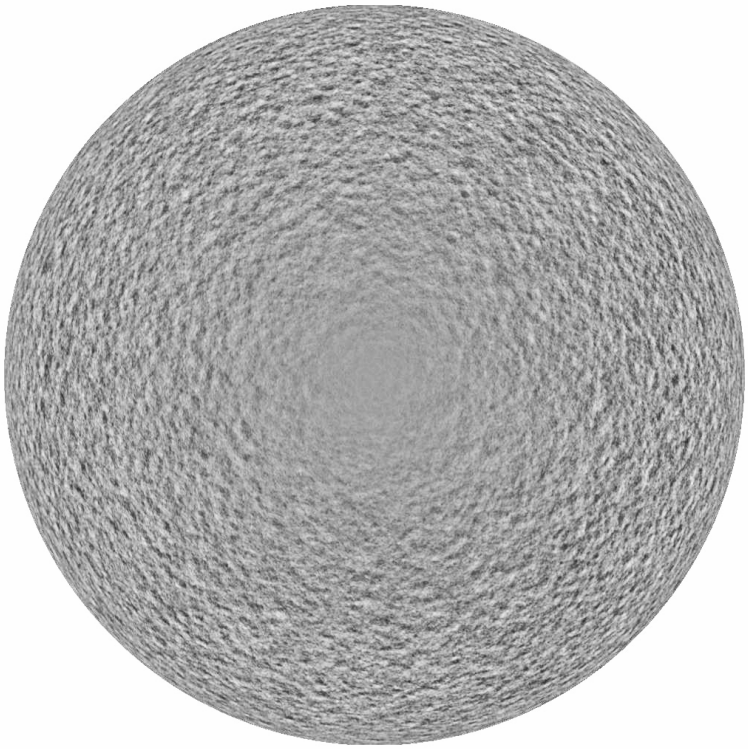

Fig. 17. The cellular flows of supergranulation as seen in full-disk MDI Doppler velocity maps (30 min average) after correction for solar (differential) rotation. Motions away from the observer are bright, motions towards the observer are dark. The flow field is dominated by the largely horizontal outflows from the centers to the edges of the supergranules with typical velocities of 300 to 500 m s^{-1}. Reproduced from [00Hat].

scale motions are primarily revealed by their horizontal advection of the smaller scale motions at the visible solar surface.

From these basic considerations, the surface velocity field is expected to have a smooth size spectrum, with velocity amplitudes that decrease steadily with increasing horizontal scale, and this behavior is in fact seen in large-scale numerical simulations ([09Ste]). Observationally, however, several distinct characteristic scales beyond the granular scale have been identified: Cellular motions with scales of the order of 10 Mm, first reported by [81Nov], are called *meso-granules*, while motions with scales of the order of 30 Mm, discovered by [56Har] and recognized as a cellular flow system by [62Lei], are called *super-granules*. Larger scale motions with dimensions of roughly 100 Mm were suggested to exist by [65Bum] and are traditionally referred to as *giant cells* (see [98Bec] for recent evidence).

While the existence of the distinct intermediate scale of mesogranulation is still under debate (for a recent summary and critical discussion of mesogranulation measurements see [00Rie, 00Hat, 00Shi], and references therein), supergranular structures are easily detectable away from the center of the solar disk as a long-lived pattern in maps of the line-of-sight Doppler velocity, v_D (Fig. 17). Clearly, the photospheric velocities in supergranulation are predominantly horizontal. Using full-disk observations acquired by the MDI instrument on the SOHO spacecraft, [00Hat] obtained spherical harmonic kinetic energy spectra based on the measured v_D, and found that supergranulation is associated with excess power near spherical harmonic degree $\ell = 120$, corresponding to $k = \sqrt{\ell\,(\ell+1)}/R_\odot \approx 0.17$ Mm^{-1} or $\Lambda = 2\,\pi/k \approx 4373/\ell \approx 36.4$ Mm. No signature of mesogranulation can be identified in these power spectra.

Table 13. Measurements of horizontal scale, Λ_s, and lifetime, τ_s, of the quiet Sun supergranulation.

Authors	Λ_s [Mm]	τ_s [h]	Remarks	Ref.
Hart (1956)	26	–	Oxford, AC of Doppler signal	[56Har]
Simon & Leighton (1964)	32	20	Mount Wilson, AC of Doppler signal	[64Sim]
Rimmele & Schröter (1989)	33.7 - 37.8	–	Capri, Doppler signal	[89Rim]
Wang et al. (1996)	23	–	BBSO magnetograms, AC, divergence	[96Wan]
Hagenaar et al. (1997)	13 - 18	–	South Pole, chromospheric network	[97Hag]
Hathaway et al. (2000)	36.4	–	SOHO/MDI, Full disk Doppler signal	[00Hat]
Duvall & Gizon (2000)	36.4	–	SOHO/MDI, f-mode helioseismology	[00Duv]
DeRosa & Toomre (2004)	15 - 20	16 - 23	SOHO/MDI, LCT, velocity divergence	[04DeR]
DelMoro et al. (2004)	27	22	SOHO/MDI, Local helioseismology	[04Del]
Meunier et al. (2007)	31.4	–	SOHO/MDI, LCT, velocity divergence	[07Meu1]
Rieutord et al. (2008)	36.4	–	Pic-du-Midi/CALAS, Granule tracking	[08Rie]
Hirzberger et al. (2008)	27.1	38.4	SOHO/MDI, Local helioseismology	[08Hir]
Potts & Diver (2008)	≥ 15	–	SOHO/MDI, intensity. granule tracking	[08Pot]

Supergranulation can also be detected indirectly by tracking the proper motions of surface features such as granules or magnetic bright points (e.g. [96Wan, 00Shi, 04DeR, 08Rie]). The inferred typical size of supergranulation depends on the spatial resolution of the data and on the employed data analysis techniques; classical autocorrelation methods generally give larger scales than topological methods that identify cell boundaries ([97Hag]).

The lifetime of supergranules is distributed roughly exponentially, $N(t) = N(0)\,\exp(-t/\tau_s)$, with a mean lifetime τ_s of the order of 1 day ([04DeR], [04Del, 08Hir]). Table 13 gives a non-exhaustive summary of recent measurements of the size and lifetime of solar supergranules.

The horizontal outflow velocities defining the supergranulation pattern are typically in the range 300–500 $\mathrm{m\,s^{-1}}$ (e.g. [64Sim, 89Rim, 04DeR]), and are approximately proportional to the cell size ([08Pot]). The vertical (radial) flows for typical supergranules have velocities of about 10% that of their horizontal outflows, i.e. about 30 $\mathrm{m\,s^{-1}}$ ([02Hat]).

Supergranules are barely detectable in intensity, and hence it is extremely difficult to quantify the supergranular temperature fluctuations. Until recently, all attempts at measuring these temperature variation have concluded that it must be less than 3 K across a cell ([92Lin]). Part of the difficulty in analyzing supergranular flows is that they are masked by the much stronger granulation flows. Nonetheless, elaborate measurements by [07Meu2] and [08Meu] show a small intensity contrast that would correspond to a positive temperature difference of the order of 1 K between cell centers and boundaries. These results support the view of a convective origin of supergranulation.

At chromospheric levels, supergranulation is outlined by the network-like distribution of emission in the Ca II H and K spectral lines (Fig. 18). The enhanced emission is correlated both spatially and temporally with stronger than average concentrations of quiet Sun magnetic fields, located along the edges of the supergranular cells, as first demonstrated by [64Sim]. Obviously, this distribution of magnetic flux is created by the horizontal advection of photospheric magnetic fields into the downdrafts defining the cell boundaries of the supergranulation pattern. The mainly vertical magnetic fields connect to the chromosphere where they give rise to a network of enhanced line emission.

Since the discovery of supergranulation ([56Har, 62Lei]) several attempts have been made to explain its origin. A popular idea, already proposed by [64Sim], is that a local maximum of the heat capacity, caused by the ionization of He II at a depth of roughly 20 Mm, could be responsible for driving convection cells with a preferred horizontal size that is of the same order as the depth of the He II ionization zone. Alternatively, supergranulation may be related to the spatial ordering of smaller convective cells. It has been suggested that a pattern at supergranular scales could emerge from the nonlinear collective interaction of granules ([00Rie, 03Rou]). Independent work

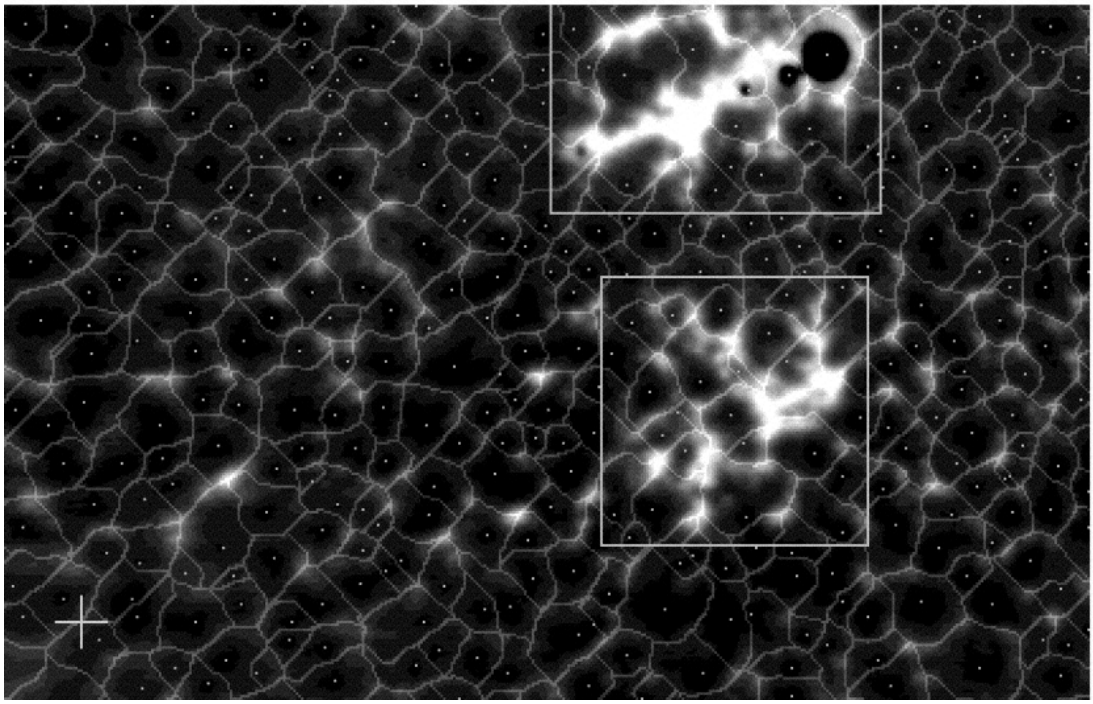

Fig. 18. Ca II K filtergram (1 nm bandpass), averaged over 8 h, showing the chromospheric network. Cell boundaries determined by a "basin-finding" algorithm are superimposed. The white boxes denote the positions of plages. The cross in the lower left corner corresponds to a size of 31×31 Mm^2. Reproduced from [97Hag].

by [07Cro], based on a numerical n-body diffusion-limited aggregation model, showed that the advection of magnetic elements by the granular flow may produce a supergranular network. The same simulation predicts that the supergranular cell size decreases with magnetic activity. The observational evidence for a variation of cell size over the solar activity cycle is still under debate ([07Meu3, 08Meu]).

Local helioseismology can be employed to study supergranular flows just below the photosphere. Using f-mode time-distance helioseismology, [00Duv] mapped supergranular flows and studied their evolution. They confirmed that the spatial power spectrum of the velocity divergence peaks at spherical harmonic degree $\ell \approx 120$. Longer time series of observations led to the discovery of the wavelike properties of supergranulation ([03Giz]), suggesting that supergranulation may be an example of traveling-wave convection. However, [06Hat] claim that the apparent supergranule superrotation is the consequence of a projection effect.

4.1.1.4.2.4 3D hydrodynamical models of the solar chromosphere

Since the 3D (magneto-)hydrodynamic simulations of solar photospheric convection described above (Section 4.1.1.4.2.2) have been very successful in reproducing observations, it would seem very natural to extend these simulations to chromospheric layers to study the effect of acoustic waves on the structure, dynamics and energetics of the chromosphere. This approach would then include both the excitation of the waves by the turbulent motions in the upper convection zone and their subsequent propagation, damping, and dissipation in chromospheric shocks. However, there are several complications that need to be addressed before this kind of modeling can be expected to yield realistic results: (i) shock formation in the chromosphere makes it necessary to

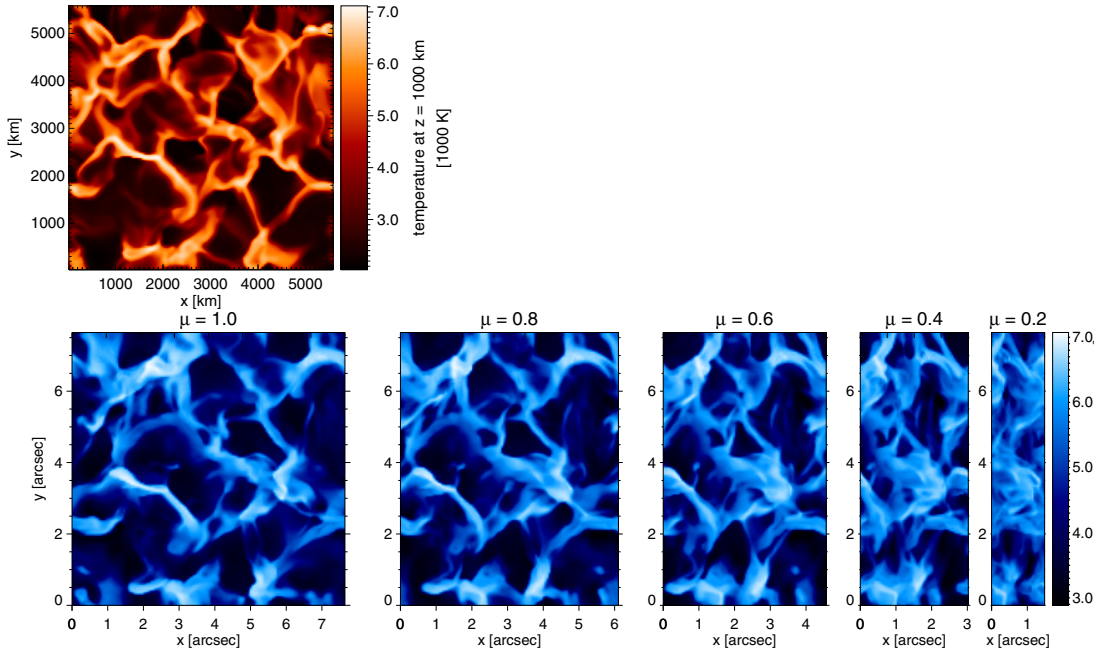

Fig. 19. (see color-picture part, page 613) Top: Gas temperature at a geometric height of z = 1000 km above $\tau_{\mathrm{Ross}} = 1$ in the non-magnetic 3D chromospheric model by [04Wed]. Temperatures range from 2000 K (black) to 7000 K (white). **Bottom:** Brightness temperature T_{b} of synthetic continuum images at λ 1 mm, computed from the snapshot shown at left for different inclination angles (μ = 1: disk-center, μ = 0.2: close to limb). T_{b} ranges from 3000 K (black) to 7000 K (white). Adapted from [07Wed3].

have a sufficiently fine grid, (ii) the approximation of LTE that works fine in the photosphere will overestimate the local coupling between gas and radiation in chromospheric layers, and (iii) it is important to take into account the long timescales for hydrogen ionization/recombination for the proper evaluation of the energy balance in the chromosphere (see Section 4.1.1.4.1.5).

3D hydrodynamic simulations extending into the chromosphere with reasonably high spatial resolution were first performed by [04Wed]. They employed only a very schematic description of the radiation (gray radiation) and did not include the effects of scattering and time-dependent hydrogen ionization. These shortcomings will surely affect the model such that a quantitative comparison with observations is not warranted. However, the qualitative results are certainly interesting: the chromosphere in these simulations is very dynamic and filamentary. Hot gas coexists with cool gas at all heights. and the gas is in the cool state a large fraction of the time. As was the case in the 1D models by [95Car], the average *gas temperature* shows very little increase with height, while the equivalent *radiation temperature* exhibits a chromospheric rise similar to the VAL C model. The temperature variations are large: at a height of 800 km, temperatures range from 2000 K in expanding regions up to 7000 K in the shocks (Fig. 19, top panel). Presumably, the amplitude of the temperature fluctuations is overestimated due to the simplifications inherent in this model. Nonetheless, the model has been used by [07Wed3] to predict the appearance of the mid chromosphere as seen at mm wavelength at high spatial resolution (bottom panels of Fig. 19) for comparison with future ALMA observations. Similar patterns are also visible in the magnetic follow-up models ([05Sch, 06Sch, 08Ste], as summarized in [07Ste2]), and in the more advanced flux tube emergence simulations by [08Mar] that extend from the convection zone into the corona.

The low temperatures in the simulations allow for a large amount of CO molecules to be present at chromospheric heights, consistent with observations. For a proper calculation of CO concentrations it is important to take into account the detailed chemical network of CO formation, including

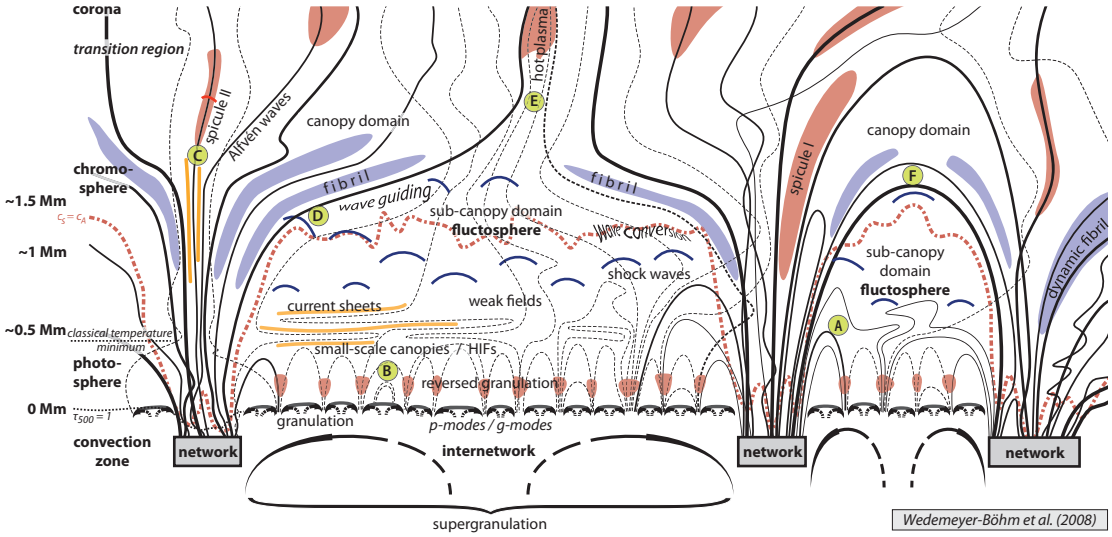

Fig. 20. (see color-picture part, page 614) Schematic, simplified structure of the lower atmosphere of the quiet Sun (dimensions not to scale). Reproduced from [09Wed1].

the timescales of the reactions. Incorporating the dynamic CO formation in 2D simulations and considering the radiative cooling of the infrared CO lines in the energy balance, [07Wed2] showed that CO-cooling is unlikely to play an active role in controlling the thermal structure at chromospheric heights, as long as these layers are highly dynamic.

Indeed, recent observations now prove – beyond any doubt– the chromosphere to be a highly dynamic and intermittent layer structured by magnetic fields (e.g. [3, 06Jud, 06Noo, 06Woe, 09Vec]). The chromosphere may well be the most complex layer of the Sun. The *modern view* of the quiet solar atmosphere, inferred from current observations and numerical simulations, is sketched in Fig. 20.

The network magnetic field is concentrated at the borders of the supergranulation cells, which are the result of large-scale convective flows (large arrows at the bottom). The magnetic field lines that originate in the network in the lower photosphere (solid lines) expand with height. Depending on the polarity of neighboring flux concentrations, they can either form funnels or connect via loops that span the internetwork regions in-between. Above a certain height they fill the entire volume, forming a large-scale "canopy" field above the internetwork regions. In this way, the atmosphere is "separated" into a "canopy domain" (upper chromosphere) and a "sub-canopy domain" (low and mid chromosphere). The canopy domain is dominated by (large-scale) magnetic fields. It is this layer which, due to the emission in Hα, appears as a purple-red rim at the beginning and end of a total solar eclipse. The sub-canopy domain is characterized by mostly weak magnetic fields that are passively advected by the hydrodynamic flow fields.

The internetwork regions are not absolutely field-free, as indicated by the field lines with footpoints in the internetwork (thin dashed lines). The convective flows on smaller spatial scales (small arrows) produce the granulation pattern at the bottom of the photosphere ($z = 0$ Mm) and, through convective overshooting, are responsible for the generation of the weak-field "small-scale canopies" in the internetwork. Another consequence of overshooting is the formation of the reversed granulation pattern in the middle photosphere (red areas). The predominantly weak field in the internetwork can emerge as small magnetic loops, even within a granule (point **B**). It may also partially connect to the magnetic field of the upper layers in a complex manner. At the same time, the internetwork weak field may be interconnected with the network magnetic field, e.g. by

small loops which extend on granular scales (**A**).

Upward propagating, interacting shock waves (blue arches), which are excited in the layers below the classical temperature minimum, build up the "fluctosphere" (also called "clapotisphere", [3]) in the internetwork sub-canopy domain. The hypothetical surface, where sound speed and Alfvèn speed are equal is marked by the thick dotted (red) line. It is the place where wave conversion occurs, i.e. incoming acoustic waves are converted into other modes, such as fast and slow magneto-acoustic waves. In general, it can be assumed that the (acoustic) shock waves coming from the fluctosphere are guided by the magnetic canopy field (**D**). Consequently, waves might follow the canopy field upwards and compress and heat the gas trapped between chromospheric "funnels" (**E**). In closed loop regions, strong waves could push into the canopy from below and compress the magnetic field (**F**). Label **C** indicates the generation of type-II spicules in the upper chromosphere, located above some vertically oriented current sheets.

In reality, the 3D magnetic field structure in the canopy and also in the subcanopy is certainly more complex and entangled than shown in this simplified schematic sketch. Despite great progress on the theoretical and observational sides, a comprehensive picture of the quiet Sun atmosphere is still missing. The nature of the heating mechanism of the quiet Sun chromosphere remains at the heart of the open questions.

4.1.1.4.3 References for 4.1.1.4

Monographs

a Böhm, K.-H.: Landolt-Börnstein, NS, Vol. VI/1 (1965) p. 99.

b Bray, R.J., Loughhead, R.E., Durrant, C.J.: The solar granulation, 2nd ed., Cambridge and New York, Cambridge University Press (1984).

c Cox, A.N., Livingston, W.C., Matthews, M.S. (eds.): Solar interior and atmosphere, University of Arizona Press (1991).

d Lites, B.W. (ed.): Chromospheric Diagnostics and Modelling, Sunspot, NM, National Solar Observatory (1985).

e Durrant, C.J.: Landolt-Börnstein, NS, Vol. VI/2a, Astronomy and Astrophysics (K. Schaifers, H.H. Voigt, eds.), Berlin, Heidelberg, New York: Springer-Verlag (1981) p. 96.

f Durrant, C.J.: Landolt-Börnstein, NS, Vol. VI/3a, Astronomy and Astrophysics (H.H. Voigt, ed.), Berlin, Heidelberg, New York: Springer-Verlag (1993) p. 89.

g Rutten, R.J., Severino, G. (eds.): Solar and stellar granulation, Dordrecht: Kluwer, (1989)

h Stix, M.: The Sun. An introduction, 2nd edition, Astronomy and Astrophysics Library, Berlin: Springer-Verlag (2004).

i Sturrock, P.A., Holzer, T.E., Mihalas, D.M., Ulrich, R K. (eds.): Physics of the sun. Volume 2. The solar atmosphere, Dordrecht, D. Reidel Publishing Co. (1986).

j Waldmeier, M.: Landolt-Börnstein, NS, Vol. VI/1 (1965) p. 112.

k Foukal, P.V.: Solar astrophysics, 2nd revised edition, Wiley (2004).

l Cox, A.N., Livingston, W.C., Matthews, M.S. (editors): Solar Interior and Atmosphere, The University of Arizona Press, Tucson (1991).

Reviews

0 Solanki, S.K., Hammer, R.: "The solar atmosphere", in The Century of Space Science (J.A. Bleeker, J. Geiss, M. Huber, eds.), Berlin: Springer-Verlag (2002) p. 1065–1088.

1 Gustafsson, B., Jørgensen, U.G.: Astron. Astrophys. Rev. (1994) 6, p. 19–65.

2 Spruit, H.C., Nordlund, Å., Title, A.M.: Annu. Rev. Astron. Astrophys. (1990) 28, p. 263–301.

3 Rutten, R.: "Observing the Solar Chromosphere", in: The Physics of Chromospheric Plasmas (P. Heinzel, I. Dorotovič, R.J. Rutten, eds.), ASP Conference Series, Vol. 368 (2007) p. 27.
4 Carlsson, M.: "Modeling the Solar Chromosphere", in The Physics of Chromospheric Plasmas (P. Heinzel, I. Dorotovič, R.J. Rutten, eds.), ASP Conference Series, Vol. 368 (2007) p. 49.
5 Brandt, P.N.: in Encyclopedia of Astronomy and Astrophysics, (P. Murdin, ed.), Nature Publishing Group and Institute of Physics, **Vol. III** (2000) 2659.

Special references

53Syk Sykes, J.B.: Mon. Not. R. astr. Soc. **113** (1953) 198.
53Ube Uberoi, M.S., Kovasznay, L.S.: Quart. Appl. Math **10** (1953) 392.
55Fre Frenkiel, F.N., Schwarzschild, M.: Astrophys. J. **121** (1955) 216.
55Ube Uberoi, M.S.: Astrophys. J. **122** (1955) 466.
56Har Hart, A.B.: Mon. Not. R. astr. Soc. **116** (1956) 38.
58Boe Böhm-Vitense, E.: Z. Astrophys. **46** (1958) 108.
59Gol Goldberg, L., Pierce, A.K.: Handbuch der Physik **52** (1959) 1.
59Sch Schwarzschild, M.: Astrophys. J. **130** (1959) 345.
61Bah Bahng, J., Schwarzschild, M.: Astrophys. J. **134** (1961) 337.
62Lei Leighton, R.B., Noyes, R.W., Simon, G.W.: Astrophys. J. **135** (1962) 474.
64Sim Simon, G.W., Leighton, R.B.: Astrophys. J. **140** (1964) 1120.
65Bum Bumba, V., Howard, R.: Astrophys. J. **141** (1965) 1502.
65Hen Henyey, L., Vardya, M. S., Bodenheimer, P.: Astrophys. J. **142** (1965) 841.
67Hol Holweger, H.: Zeitschrift für Astrophysik **65** (1967) 365.
68Cox Cox, J.P., Giuli, R.T.: Principles of Stellar Structure, Vol. 1, Gordon and Breach (1968).
69Bec Beckers, J.M., Parnell, R.L.: Solar Phys. **9** (1969) 39.
69Nam Namba, O., Diemel, W.E.: Solar Phys. **7** (1969) 167.
70Kur Kurucz, R.L.: ATLAS: A computer program for calculating model stellar atmospheres, Smithonian Astrophysical Observatory, Special Report 309 (1970).
71Lev L'evy, M.: Astron. Astrophys. **14** (1971) 15.
71Meh1 Mehltretter, J.P.: Solar Phys. **16** (1971) 253.
71Meh2 Mehltretter, J.P.: Solar Phys. **19** (1971) 32.
72Noy Noyes, R.W., Hall, D.N.B.: Astrophys. J. **176** (1972) L89.
73Can Canfield, R.C., Mehltretter, J.P.: Solar Phys. **33** (1973) 33.
74Hol Holweger, H., Müller, E.A.: Solar Phys. **39** (1974) 19.
74Kur Kurucz, R.L.: Solar Phys. **34** (1974) 17.
75Deu Deubner, F.L., Mattig, W.: Astron. Astrophys. **45** (1975) 167.
75Gus Gustafsson B., Bell, R.A., Eriksson K., Nordlund, Å.: Astron. Astrophys. **42** (1975) 407.
77Edm Edmonds, F.N., Hinkle, K.H.: Solar Phys. **51** (1977) 273.
77Kar Karpinsky, V.N., Mekhanikov, V.V.: Solar Phys. **54** (1977) 25.
77Kei Keil, S.L.: Solar Phys. **53** (1977) 359.
77Ulm Ulmschneider, P., Kalkofen, W., Nowak, T., Bohn, U.: Astron. Astrophys. **54** (1977) 61.
77Wit Wittmann, A., Mehltretter, J.P.: Astron. Astrophys. **61** (1977) 75.
78Mih Mihalas, D.: Stellar Atmospheres, 2nd edition, Freeman and Company (1978).
79Kur Kurucz, R.L.: Astrophys. J. Suppl. Ser. **40** (1979) 1.
79Ric Ricort, G., Aime, C.: Astron. Astrophys. **76** (1979) 324.
79Sch Schmidt, W., Deubner, F.-L., Mattig, W., Mehltretter, J.P.: Astron. Astrophys. **75** (1979) 223.

79Wit Wittmann, A.: in Small scale motions on the sun, Mitteilungen aus dem Kiepenheuer-Institut **179** (1979) 29.
80Kne Kneer, F.: Astron. Astrophys. **87** (1980) 229.
81Avr Avrett, E.H.: in Solar phenomena in stars and stellar systems, (R.M.Bonnet and A.K. Dupree, eds.), Dordrecht, D. Reidel Publishing Co. (1981) p. 173.
81Ayr1 Ayres, T.R.: Astrophys. J. **244** (1981) 1064.
81Ayr2 Ayres, T.R., Testerman, L.: Astrophys. J. **245** (1981) 1124.
81Dra Dravins, D., Lindegren, L., Nordlund, Å.: Astron. Astrophys. **96** (1981) 345.
81Nov November, L.J., Toomre, J., Gebbie, K.B., Simon, G.W.: Astrophys. J. **245** (1981) L123.
81Ric Ricort, G., Aime, C., Deubner, F., Mattig, W.: Astron. Astrophys. **97** (1981) 114.
81Sch Schmidt, W., Knoelker, M., Schroeter, E.H.: Solar Phys. **73** (1981) 217.
81Ver Vernazza, J.E., Avrett, E.H., Loeser, R.: Astrophys. J. Suppl. Ser. **45** (1981) 635.
82Dra Dravins, D.: Annu. Rev. Astron. Astrophys. (1982) 20, p. 61–89.
82Nor Nordlund, Å.: Astron. Astrophys. **107** (1982) 1.
83Dur Durrant, C.J., Mattig, W., Nesis, A., Schmidt, W.: Astron. Astrophys. **123** (1983) 319.
83Kne Kneer, F.: Astron. Astrophys. **128** (1983) 311.
83Mac Macris, C., Rösch, J.: C.R. Acad. Sci Paris **296** (1983) 265.
84Nor1 Nordlund, Å.: in Small-Scale Dynamical Processes in Quiet Stellar Atmospheres, (S.L. Keil, ed.), National Solar Observatory (1984) 181.
84Nor2 Nordlund, Å.: in Small-Scale Dynamical Processes in Quiet Stellar Atmospheres, (S.L. Keil, ed.), National Solar Observatory (1984) 174.
85Avr Avrett, E.H.: in Chromospheric Diagnostics and Modelling, (B.W. Lites, ed.) Sunspot, NM, National Solar Observatory (1985) p. 67.
85Nor Nordlund, Å.: Solar Phys. **100** (1985) 209.
86Ayr Ayres, T.R., Testerman, L., Brault, J.W.: Astrophys. J. **304** (1986) 542.
86Dra Dravins, D., Larsson, B., Nordlund, Å.: Astron. Astrophys. **158** (1986) 83.
86Mal Maltby, P., Avrett, E.H., Carlsson, M., Kjeldseth-Moe, O., Kurucz, R.L., Loeser, R.: Astrophys. J. **306** (1986) 284.
86Rou1 Roudier, T., Muller, R.: Solar Phys. **107** (1986) 11.
86Rou2 Roudier, T.: Thesis, Université Sabatier, Toulouse, France (1986).
87Col Collados, M., Vázquez, M.: Astron. Astrophys. **180** (1987) 223.
87Lue von der Lühe, O., Dunn, R.B.: Astron. Astrophys. **177** (1987) 265.
89And1 Anderson, L.S.: Astrophys. J. **339** (1989) 558.
89And2 Anderson, L.S., Athay, R.G.: Astrophys. J. **346** (1989) 1010.
89And3 Anderson, L.S., Athay, R.G.: Astrophys. J. **336** (1989) 1089.
89Ayr Ayres, T.R., Wiedemann, G.R.: Astrophys. J. **338** (1989) 1033.
89Dar Darvann, T.A., Kusoffsky, U.: in Solar and stellar granulation (R.J. Rutten, G. Severino, eds.), Dordrecht: Kluwer (1989) 313.
89Lit Lites, B.W., Nordlund, Å., Scharmer, G.B.: in Solar and stellar granulation (R.J. Rutten, G. Severino, eds.), Dordrecht: Kluwer (1989) 349.
89Mul Muller, R.: in Solar and stellar granulation (R.J. Rutten, G. Severino, eds.), Dordrecht: Kluwer (1989) 101.
89Rim Rimmele, T., Schröter, E.H.: Astron. Astrophys. **221** (1989) 137.
89Ste Stein, R.F., Nordlund, Å.: Astrophys. J. **342** (1989) L95.
89Tit Title, A.M., Tarbell, T.D., Topka, K.P., Ferguson, S.H., Shine, R.A., and the SOUP Team: Astrophys. J. **336** (1989) 475.
90Ayr Ayres, T.R., Brault, J.W.: Astrophys. J. **363** (1990) 705.
90Fon Fontenla, J.M., Avrett, E.H., Loeser, R.: Astrophys. J. **355** (1990) 700.
91Fon Fontenla, J.M., Avrett, E.H., Loeser, R.: Astrophys. J. **377** (1991) 712.

91Kel Keller, C.U., Koutchmy, S.: Astrophys. J. **379** (1991) 751.
91Kom Komm, R., Mattig, W., Nesis, A.: Astron. Astrophys. **243** (1991) 251.
91Ste Steffen, M., Freytag, B.: in Reviews in Modern Astronomy, (G. Klare, ed.), **4** (1991) 43.
92Car Carlsson M., Stein R.F.: Astrophys. J. **397** (1992) L59.
92Lin Lin, H., Kuhn, J.R.: Solar Phys. **141** (1992) 1.
92Rod Rodriguez Hidalgo, I., Collados, M., Vázquez, M.: Astron. Astrophys. **264** (1992) 661.
93Esp Espagnet, O., Muller, R., Roudier, T., Mein, N.: Astron. Astrophys. **271** (1993) 589.
93Fon Fontenla, J.M., Avrett, E.H., Loeser, R.: Astrophys. J. **406** (1993) 319.
94Atr Atroshchenko, I.N., Gadun, A.S.: Astron. Astrophys. **291** (1994) 635.
94Nec Neckel, H., Labs, D.: Solar Phys. **153** (1994) 91.
95Car Carlsson M., Stein R.F., Astrophys. J. **440** (1995) L29.
95Esp Espagnet, O., Muller, R., Roudier, T., Mein, N., Mein, P.: Astron. Astrophys. Suppl. **109** (1995) 79.
95Gad Gadun, A.S., Vorob'yov, Y.Y.: Solar Phys. **159** (1995) 45.
96Col Collados, M., Rodriguez Hidalgo, I., Ballesteros, E., Ruiz Cobo, B., Sanchez Almeida, J., del Toro Iniesta, J.C.: Astron. Astrophys. Suppl. **115** (1996) 367.
96Nec Neckel, H.: Solar Phys. **167** (1996) 9.
96Wan Wang, H., Tang, F., Zirin, H., Wang, J.: Solar Phys. **165** (1996) 223.
97Car Carlsson, M., Stein, R.F.: Astrophys. J. **481** (1997) 500.
97Gad Gadun, A.S., Hanslmeier, A., Pikalov, K.N.: Astron. Astrophys. **320** (1997) 1001.
97Hag Hagenaar, H.J., Schrijver, C.J., Title, A.M.: Astrophys. J. **481** (1997) 988.
97Hir Hirzberger, J., Váazquez, M., Bonet, J.A., Hanslmeier, A., Sobotka, M.: Astrophys. J. **480** (1997) 406.
97Nor Nordlund, Å., Spruit, H.C., Ludwig, H.-G., Trampedach, R.: Astron. Astrophys. **328** (1997) 229.
97Sch Schrijver, C.J., Hagenaar, H.J., Title, A.M.: Astrophys. J. **475** (1997) 328.
97Wil Wilken, V., de Boer, C.R., Denker, C., Kneer, F.: Astron. Astrophys. **325** (1997) 819.
98Bec Beck, J.G., Duvall Jr., T.L., Scherrer, P.H.: Nature **394** (1998) 653.
98Gre Grevesse, N., Sauval, A.J.: Space Science Reviews **85** (1998) 161.
98Hes Hestroffer, D., Magnan, C.: Astron. Astrophys. **333** (1998) 338.
98Ste Stein, R.F., Nordlund, Å., Astrophys. J. **499** (1998) 914.
99Cat Cattaneo, F.: Astrophys. J. **515** (1999) L39.
99Fon Fontenla, J.M., White, O.R., Fox, P.A., Avrett, E.H., Kurucz, R.L.: Astrophys. J. **518** (1999) 480.
99Gre Grevesse, N., Sauval, A.J.: Astron. Astrophys. **347** (1999) 348.
99Hir Hirzberger, J., Bonet, J.A., Vázquez, M., Hanslmeier, A.: Astron. Astrophys. **515** (1999) 441.
99Kal Kalkofen, W., Ulmschneider, P., Avrett, E.H.: Astrophys. J. **521** (1999) L141.
99Kri Krieg, J., Wunnenberg, M., Kneer, F., Koschinsky, M., Ritter, C.: Astron. Astrophys. **343** (1999) 983.
99Lud Ludwig, H.-G., Freytag, B., Steffen, M.: Astron. Astrophys. **346** (1999) 111.
99Mul Muller, R.: in Motions in the Solar Atmosphere, (A. Hanslmeier and M. Messerotti, eds.), ASSL **239** (1999) 35.
00Asp1 Asplund, M., Ludwig, H.-G., Nordlund, Å., Stein, R.F.: Astron. Astrophys. **359** (2000) 669.
00Asp2 Asplund, M., Nordlund, Å., Trampedach, R., Allende Prieto, C., Stein, R.F.: Astron. Astrophys. **359** (2000) 729.
00Asp3 Asplund, M., Nordlund, Å., Trampedach, R., Stein, R.F.: Astron. Astrophys. **359** (2000) 743.

00Asp4 Asplund, M.: Astron. Astrophys. **359** (2000) 755.
00Duv Duvall, T.L., Gizon, L.: Solar Phys. **192** (2000) 177.
00Hat Hathaway, D.H., Beck, J.G., Bogart, R.S., Bachmann, K.T., Khatri, G., Petitto, J.M., Han, S., Raymond, J.: Solar Phys. **193** (2000) 299.
00Kri Krieg, J., Kneer, F., Koschinsky, M., Ritter, C.: Astron. Astrophys. **360** (2000) 1157.
00Rie Rieutord, M., Roudier, T., Malherbe, J.M., Rincon, F.: Astron. Astrophys. **357** (2000) 1063.
00Ste Stein, R.F., Nordlund, Å.: Solar Phys. **192** (2000) 91.
00San Sánchez Cuberes, M., Bonet, J.A., Vázquez, M., Wittmann, A.D.: Astrophys. J. **538** (2000) 940.
00Shi Shine, R.A., Simon, G.W., Hurlburt, N.E.: Solar Phys. **193** (2000) 313.
00Uit Uitenbroek, H.: Astrophys. J. **536** (2000) 481.
01Hir Hirzberger, J., Koschinsky, M., Kneer, F., Ritter, C.: Astron. Astrophys. **367** (2001) 1011.
01Mue Müller, D.A.N., Steiner, O., Schlichenmaier, R., Brandt, P.N.: Solar Phys. **203** (2001) 211.
01Nor Nordlund, Å., Stein, R.F.: Astrophys. J. **546** (2001) 576.
01Ste Stein, R.F., Nordlund, Å., Astrophys. J. **546** (2001) 585.
02Ayr Ayres, T.R.: Astrophys. J. **575** (2002) 1104.
02Car1 Carlsson, M., Stein R.F.: Astrophys. J. **572** (2002) 626.
02Car2 Carlsson, M., Stein R.F.: in SOHO-11: From Solar Minimum to Maximum, (A. Wilson, ed.), ESA SP-508 (2002) 245.
02Cow Cowley, C.R., Castelli, F.: Astron. Astrophys. **387** (2002) 595.
02Fon Fontenla, J.M., Avrett, E.H., Loeser, R.: Astrophys. J. **572** (2002) 636.
02Fre Freytag, B., Steffen, M., Dorch, B.: Astron. Nachr. **323** (2002) 213.
02Hei Heiter, U., Kupka, F., van't Veer-Menneret, C., Barban, C., Weiss, W.W., Goupil, M.-J., Schmidt, W., Katz, D., Garrido, R.: Astron. Astrophys. **392** (2002) 619.
02Hat Hathaway, D.H., Beck, J.G., Han, S., Raymond, J.: Solar Phys. **205** (2002) 25.
03Cat Cattaneo, F., Emonet, T., Weiss, N.: Astrophys. J. **588** (2003) 1183.
03Gus Gustafsson, B., Edvardsson, B., Eriksson, K., Mizuno-Wiedner, M., Jørgensen, U.G., Plez, B.: in Stellar Atmosphere Modeling, (I. Hubeny, D. Mihalas, K. Werner, eds.), ASP Conference Proceedings Vol. **288** (2003) 331.
03Giz Gizon, L., Duvall, T.L., Schou, J.: Nature **421** (2003) 43.
03Liv Livingston, W., Wallace, L.: Solar Phys. **212** (2003) 227.
03Nec Neckel, H.: Solar Phys. **212** (2003) 239.
03Pus Puschmann, K., Vázquez, M., Bonet, J.A., Ruiz Cobo, B., Hanslmeier, A.: Astron. Astrophys. **408** (2003) 363.
03Rou Roudier, T., Lignières, F., Rieutord, M., Brandt, P.N., Malherbe, J.M.: Astron. Astrophys. **409** (2003) 299.
03Sam Samadi, R., Nordlund, Å., Stein, R.F., Goupil, M.-J., Roxburgh, I.: Astron. Astrophys. **404** (2003) 1129.
03Ulm Ulmschneider, P., Musielak, Z.: in Current Theoretical Models and Future High Resolution Solar Observations: Preparing for ATST, (A.A. Pevtsov, H. Uitenbroek, eds.), ASP Conference Series **286** (2003) 363.
04Asp Asplund, M., Grevesse, N., Sauval, A.J., Allende Prieto, C., Kiselman, D.: Astron. Astrophys. **417** (2004) 751.
04Car Carlsson, M., Stein, R.F., Nordlund, Å., Scharmer, G.B.: Astrophys. J. **610** (2004) L137.
04Del Del Moro, D., Berrilli, F., Duvall, T.L., Kosovichev, A G.: Solar Phys. **221** (2004) 23.
04DeR DeRosa, M.L., Toomre, J.: Astrophys. J. **616** (2004) 1242.

04Ste Stein, R., Georgobiani, D., Trampedach, R., Ludwig, H.-G., Nordlund, Å.: Solar Phys. **220** (2004) 229.
04Tru Trujillo Bueno, J., Shchukina, N., Asensio Ramos, A.: Nature **430** (2004) 326.
04Wed Wedemeyer, S., Freytag, B., Steffen, M., Ludwig, H.-G., Holweger, H.: Astron. Astrophys. **414** (2004) 1121.
05Asp Asplund, M., Grevesse, N., Sauval, A.J.: in Cosmic Abundances as Records of Stellar Evolution and Nucleosynthesis, ASP Conf. Ser. **336** (2005) 25.
05Bah1 Bahcall, J.N., Basu, S., Pinsonneault, M., Serenelli, A.: Astrophys. J. **618** (2005) 1049.
05Bah2 Bahcall, J.N., Serenelli, A., Basu, S.: Astrophys. J. **621** (2005) L85.
05Fos1 Fossum, A., Carlsson, M.: Astrophys. J. **625** (2005) 556.
05Fos2 Fossum, A., Carlsson, M.: Nature **435** (2005) 919.
05Kur Kurucz, R.L.: Mem. S.A.It. Suppl. Vol. **8** (2005) 14.
05Nec Neckel, H.: Solar Phys. **229** (2005) 13.
05Pus Puschmann, K.G., Ruiz Cobo, B., Vázquez, M., Bonet, J.A., Hanslmeier, A.: Astron. Astrophys. **441** (2005) 1157.
05Sch Schaffenberger, W., Wedemeyer-Böhm, S., Steiner, O., Freytag, B.: in Magnetohydrodynamic Simulation from the Convection Zone to the Chromosphere, (D.E. Innes, A. Lagg, S.A. Solanki, eds.), ESA Special Publication **596** (2005) 65.
05Sho Short, C.I., Hauschildt, P.H.: Astrophys. J. **618** (2005) 926.
05Ulm Ulmschneider, P., Rammacher, W., Musielak, Z.E., Kalkofen, W.: Astrophys. J. **631** (2005) L155.
05Voe Vögler, A., Shelyag, S., Schüssler, M., Cattaneo, F., Emonet, T., Linde, T.: Astron. Astrophys. **429** (2005) 335.
06Ant Antia, H.M., Basu, S.: Astrophys. J. **644** (2006) 1292.
06Ayr Ayres, T.R., Plymate, C., Keller, C.U.: Astrophys. J. Suppl. Ser. **165** (2006) 618.
06Fon Fontenla, J.M., Avrett, E.H., Thuillier, G., Harder, J.: Astrophys. J. **639** (2006) 441.
06Fos Fossum, A., Carlsson, M.: Astrophys. J. **646** (2006) 579.
06Hat Hathaway, D. H., Williams, P.E., Cuntz, M.: Astrophys. J. **644** (2006) 598.
06Jud Judge, P.: in Solar MHD Theory and Observations: A High Spatial Resolution Perspective, (J. Leibacher, R.F. Stein, H. Uitenbroek, eds.), Astronomical Society of the Pacific Conference Series **354** (2006) 259.
06Nes Nesis, A., Hammer, R., Roth, M., Schleicher, H.: Astron. Astrophys. **451** (2006) 1081.
06Noo van Noort, M.J., Rouppe van der Voort, L.H.M.: Astrophys. J. **648** (2006) L67.
06Sch Schaffenberger, W., Wedemeyer-Böhm, S., Steiner, O., Freytag, B.: in Solar MHD Theory and Observations: A High Spatial Resolution Perspective, (J. Leibacher, R.F. Stein, H. Uitenbroek, eds.), Astronomical Society of the Pacific Conference Series **354** (2006) 345.
06Ste1 Stein, R.F., Nordlund, Å.: Astrophys. J. **642** (2006) 1246.
06Ste2 Stein, R.F., Benson, D., Georgobiani, D., Nordlund, Å.: in Proceedings of SOHO 18/GONG 2006/HELAS I, Beyond the spherical Sun, ESA Special Publication **624** (2006) 79.
06Woe Wöger, F., Wedemeyer-Böhm, S., Schmidt, W., von der Lühe, O.: Astron. Astrophys. **459** (2006) L9.
07Cro Crouch, A.D., Charbonneau, P., Thibault, K.: Astrophys. J. **662** (2007) 715.
07Els Elste, G., Gilliam, L.: Solar Phys. **240** (2007) 9.
07Fon Fontenla, J.M., Balasubramaniam, K.S., Harder, J.: Astrophys. J. **667** (2007) 1243.
07Gre Grevesse, N., Asplund, M., Sauval, A.J.: Space Sci. Rev. **130** (2007) 105.
07Ham Hammer, R., Ulmschneider, P.: in Chromospheric Dynamics and Line Formation, (S.S. Hasan, D. Banerjee, eds.), AIP Conference Series **919** (2007) 138.
07Meu1 Meunier, N., Tkaczuk, R., Roudier, T., Rieutord, M.: Astron. Astrophys. **461** (2007) 1141.

07Meu2 Meunier, N., Tkaczuk, R., Roudier, T.: Astron. Astrophys. **463** (2007) 745.
07Meu3 Meunier, N., Roudier, T., Tkaczuk, R.: Astron. Astrophys. **466** (2007) 1123.
07Mul Muller, R., Hanslmeier, A., Saldaña-Muñoz, M.: Astron. Astrophys. **475** (2007) 717.
07Ram Rammacher, W., Schmidt, W., Hammer, R.: in The Physics of Chromospheric Plasmas, (P. Heinzel, I. Dorotovič, R.J. Rutten, eds.), ASP Conference Series, Vol. 368 (2007) p. 147.
07Ste1 Steffen, M.: in Convection in Astrophysics, (F. Kupka, I.W. Roxburgh, K.L. Chan, eds.), Proc. IAU Symp. No. 239 (2007) 36.
07Ste2 Steiner, O.: in Kodai School on Solar Physics, (S.S. Hasan, D. Banerjee, eds.), AIP Conference Series **919** (2007) 74.
07Uit Uitenbroek, H., Tritschler, A., Rimmele, T.: Astrophys. J. **668** (2007) 586.
07Voe Vögler, A., Schüssler, M.: Astron. Astrophys. **465** (2007) L43.
07Wed1 Wedemeyer-Böhm, S., Steiner, O., Bruls, J., Rammacher, W.: in The Physics of Chromospheric Plasmas, (P. Heinzel, I. Dorotovič, R.J. Rutten, eds.), ASP Conference Series, Vol. 368 (2007) p. 93.
07Wed2 Wedemeyer-Böhm, S., Steffen, M.: Astron. Astrophys. **462** (2007) L31.
07Wed3 Wedemeyer-Böhm, S., Ludwig, H.-G., Steffen, M., Leenaarts, J., Freytag, B.: Astron. Astrophys. **471** (2007) 977.
08Avr Avrett, E.H., Loeser, R.: Astrophys. J. Suppl. Ser. **175** (2008) 229.
08Bas Basu, S., Antia, H.M.: Phys. Rep. **457** (2008) 217.
08Caf Caffau, E., Ludwig, H.-G., Steffen, M., Ayres, T.R., Bonifacio, P., Cayrel, R., Freytag, B., Plez, B.: Astron. Astrophys. **488** (2008) 1031.
08Dan Danilovic, S., Gandorfer, A., Lagg, A., Schüssler, M., Solanki, S.K., Vögler, A., Katsukawa, Y., Tsuneta, S.: Astron. Astrophys. **484** (2008) L17.
08Dra Dravins, D.: Astron. Astrophys. **492** (2008) 199.
08Gus Gustafsson, B., Edvardsson, B., Eriksson, K., Gråe Jørgensen, U., Nordlund, Å. Plez, B.: Astron. Astrophys. **486** (2008) 951.
08Hir Hirzberger, J., Gizon, L., Solanki, S.K., Duvall, T.L.: Solar Phys. **251** (2008) 417.
08Kis Kiselman, D.: Physica Scripta Volume T **133** (2008) 014016.
08Liv Livingston, W., Sheeley, N.R.: Astrophys. J. **672** (2008) 1228.
08Mar Martinez-Sykora, J., Hansteen, V., Carlsson, M.: Astrophys. J. **679** (2008) 871.
08Meu Meunier, N., Roudier, T., Rieutord, M.: Astron. Astrophys. **488** (2008) 1109.
08Pot Potts, H.E., Diver, D.A.: Solar Phys. **248** (2008) 263.
08Rie Rieutord, M., Meunier, N., Roudier, T., Rondi, S., Beigbeder, F., Parès, L.: Astron. Astrophys. **479** (2008) L17.
08Ste Steiner, O., Rezaei, R., Schaffenberger, W., Wedemeyer-Böhm, S.: Astrophys. J. **680** (2008) L85.
08Str Straus, T., Fleck, B., Jefferies, S.M., Cauzzi, G., McIntosh, S. W., Reardon, K., Severino, G., Steffen, M.: Astrophys. J. **681** (2008) L125.
08Wed Wedemeyer-Böhm, S.: Astron. Astrophys. **487** (2008) 399.
09Lud Ludwig, H.-G., Steffen, M., Freytag, B., Caffau, E., Bonifacio, P., Plez, B.: Astron. Astrophys. (2009)
09Sho Short, C.I., Hauschildt, P.H.: Astrophys. J. **691** (2009) 1634.
09Ste Stein, R.F., Georgobiani, D., Schaffenberger, W., Nordlund, Å., Benson, D.: American Institute of Physics Conference Series **1094** (2008) 764.
09Vec Vecchio, A., Cauzzi, G., Reardon, K.P.: Astron. Astrophys. **494** (2009) 269.
09Wed1 Wedemeyer-Böhm, S., Lagg, A., Nordlund, Å.: Space Sci. Rev. 144 (2009) 317.
09Wed2 Wedemeyer-Böhm, S., Rouppe van der Voort, L.: Astron. Astrophys. (2009) in press.